MOX-Report No. 18/2016

Dispersion-dissipation analysis of 3D continuous and discontinuous spectral element methods for the elastodynamics equation

Ferroni, A.; Antonietti, P.F.; Mazzieri, I.; Quarteroni, A.

MOX, Dipartimento di Matematica
Politecnico di Milano, Via Bonardi 9 - 20133 Milano (Italy)

mox-dmat@polimi.it http://mox.polimi.it

Dispersion-dissipation analysis of 3D continuous and discontinuous spectral element methods for the elastodynamics equation *

A. Ferroni[1], P.F. Antonietti[1], I. Mazzieri[1], A. Quarteroni[2,1(on leave)]

April 11, 2016

[1] MOX– Modellistica e Calcolo Scientifico
Dipartimento di Matematica
Politecnico di Milano
Piazza L. da Vinci 32, 20133 Milano, Italy
paola.antonietti@polimi.it, alberto.ferroni@polimi.it, ilario.mazzieri@.polimi.it

[2] Chair of Modeling and Scientific Computing (CMCS),
Mathematics Institute of Computational Science and Engineering (MATHICSE),
École Polytechnique Fédérale de Lausanne (EPFL),
Station 8, 1015 Lausanne, Switzerland.
alfio.quarteroni@epfl.ch

Keywords: Discontinuous Galerkin spectral element methods, Tetrahedral elements, Elastodynamics equation, Dispersion-dissipation analysis.

Abstract

In this paper we present a three dimensional dispersion and dissipation analysis for both the semi-discrete and the fully discrete approximation of the elastodynamics equation based on the plane wave method. For space discretization we compare different approximation strategies, namely the continuous and discontinuous spectral element method on both tetrahedral and hexahedral elements. The fully discrete scheme is then obtained exploiting a leap-frog time integration scheme. Several numerical results are presented and discussed.

1 Introduction

In the field of computational seismology the use of high-order numerical methods is essential for the study of complex wave propagation phenomena. In particular, the Spectral Element (SE) method, firstly introduced in [26], has been widely used in the simulation of elastic waves propagation [15, 20, 33], thanks to its accuracy and computational efficiency.

To handle highly heterogeneous media, e.g. strong contrast in the soil features, or in soil-structure interaction problems, flexible techniques such as the discontinuous Galerkin

*Paola F. Antonietti and Ilario Mazzieri have been partially supported by the SIR Research Grant no. RBSI14VTOS PolyPDEs: Non-conforming polyhedral finite element methods for approximation of partial differential equations funded by MIUR - Italian Ministry of Education, Universities and Research.

(DG) method, see, e.g. [31, 19], or the discontinuous Galerkin spectral element (DGSE) method [4, 2] have been set up. The DG approach (both in its high-order or spectral element version) provides accurate solutions and is well suited for parallel implementation; moreover, the local mesh size and the local polynomial approximation degree can be tailored to the region of interest, according to the mechanical properties or the geometrical features of the computational domain. For example we mention a high-order discontinuous approximation combined with an Arbitrary high order DERivatives time integration scheme proposed in [19, 13], and a a spectral discontinuous Galerkin method based on a domain decomposition approach introduced in [4]. In this latter work the discontinuities are imposed only across the macro-regions in which the domain is partitioned, differently for example from [31], where the DG approximation is applied elementwise.

Conforming and discontinuous spectral element methods are usually based on discretizations made by tensor product elements (i.e., hexahedral). However, since generating hexahedral grids for complex geometries may require a huge computational effort, in recent years spectral element methods have been extended to triangular and tetrahedral grids, see, e.g. [18, 36, 25]. In particular, high order methods for elastic wave propagation problems on triangular and tetrahedral grids can be found in [23, 24, 3].

A distinguishing feature of spectral methods is their very low dispersion and dissipation errors. Compared with other low order approximation techniques as for example finite difference or finite element methods, they therefore need a lower number of grid points per wavelength to retain the same level of accuracy [10]. The dispersion properties of spectral elements methods for elastic wave propagation problems have been analysed in [32] using a Rayleigh quotient approximation of the eigenvalue problem resulting from the dispersion analysis. The case of a DGSE approximation on quadrilateral grids has been investigated using a plane wave analysis in [11] and in [4]. In [4] a comparison with the Mortar method is also presented. A similar approach has been presented for spectral elements and DGSE approximations on triangular grids in [22], where different sets of interpolating nodes have been compared, and in [3], where the authors have used the modal boundary adapted functions proposed in [35]. All these works deal with two-dimensional model problems and show that triangular spectral elements feature dispersion and dissipation properties similar to those of the standard tensor product elements.

In this paper we propose a numerical study of dispersion and dissipation properties for the three-dimensional elastodynamics equation discretized with hexahedral and tetrahedral spectral elements, using both a continuous and a discontinuous approximation. Our analysis is based on the plane wave method and it is applied to the semi-discrete as well as the fully-discrete formulation, resulting after a leap-frog time integration. All methods we have considered provide low dispersion and dissipation effects and show similar behaviours with respect to the different parameters taken into account.

The paper is organized as follows. In Section 2 we introduce the elastodynamics problem and its weak formulation. In Section 3 we recall its semi-discrete continuous and discontinuous spectral elements approximation, as well as the fully discrete scheme resulting after leap-frog integration. In Section 4 we present the dispersion and dissipation analysis, describing the details of the plane wave method for both the continuous and the discontinuous case. Several numerical tests are then presented in Section 5 for the semi-discrete problem and in Section 6 for the fully-discrete problem, showing dispersion and dissipation errors as a function of different discretization parameters such as the polynomial degree, the mesh size, the incident angles and the time step. Finally, in Section 7 we draw some conclusions.

Throughout the paper, the Sobolev spaces of vector–valued and tensor-valued functions defined on open bounded domain $D \subset \mathcal{R}^3$ are denoted by $\mathbf{H}^m(D) = [H^m(D)]^3$ and $\mathcal{H}^m(D) = [H^m(D)]^{3\times 3}$, respectively. We will use the symbol $(\cdot\,,\cdot)_D$ to denote the standard inner product in any of the spaces $\mathbf{H}^0(D) \equiv \mathbf{L}^2(D)$ or $\mathcal{H}^0(D) \equiv \mathcal{L}^2(D)$.

2 Governing equations and weak formulation

We consider an open bounded domain $\Omega \subset \mathbb{R}^3$ with a smooth boundary $\Gamma = \partial\Omega$, decomposed into two non-intersecting portions $\Gamma_D \neq \emptyset$ and Γ_N, on which we prescribe the values of the displacement and of the external traction, respectively. Considering a temporal interval $[0, T]$, with $T > 0$, the dynamic equilibrium equation for an elastic medium subject to an external force leads to the following system

$$\begin{cases} \rho\partial_{tt}\mathbf{u} - \nabla\cdot\underline{\sigma}(\mathbf{u}) = \mathbf{f}, & \text{in}\,\Omega\times(0,T], \\ \mathbf{u} = \mathbf{0}, & \text{on}\,\Gamma_D\times(0,T], \\ \underline{\sigma}(\mathbf{u})\,\mathbf{n} = \mathbf{t}, & \text{on}\,\Gamma_N\times(0,T], \\ \mathbf{u} = \mathbf{u}_0, & \text{in}\,\Omega\times\{0\}, \\ \partial_t\mathbf{u} = \mathbf{v}_0, & \text{in}\,\Omega\times\{0\}. \end{cases} \tag{1}$$

There $\rho = \rho(\mathbf{x}) > 0 \in L^\infty(\Omega)$ is the medium density, $\mathbf{u} = \mathbf{u}(\mathbf{x}, t)$ is the displacement field, $\underline{\sigma}(\mathbf{u})$ is the stress tensor and $\mathbf{f} = \mathbf{f}(\mathbf{x}, t)$ is a (smooth enough) given external load (e.g., a seismic source). On the boundary we impose a rigidity condition on Γ_D and a (smooth enough) traction $\mathbf{t} = \mathbf{t}(\mathbf{x}, t)$ on Γ_N, respectively. Finally $\mathbf{u}_0 = \mathbf{u}_0(\mathbf{x})$ and $\mathbf{v}_0 = \mathbf{v}_0(\mathbf{x})$ are (smooth enough) initial data for the displacement and the velocity field, respectively.
We use the Hooke's law

$$\underline{\sigma}(\mathbf{u}) = \lambda\mathrm{tr}(\underline{\epsilon}(\mathbf{u})) + 2\mu\underline{\epsilon}(\mathbf{u}), \tag{2}$$

as the constitutive equation for the stress tensor $\underline{\sigma}$. In particular $\underline{\epsilon}(\mathbf{u}) = \frac{1}{2}(\nabla\mathbf{u} + \nabla^T\mathbf{u})$ is the strain tensor, $\lambda = \lambda(\mathbf{x}) \in L^\infty(\Omega)$ and $\mu = \mu(\mathbf{x}) \in L^\infty(\Omega)$ are the Lamé elastic coefficients and $\mathrm{tr}(\cdot)$ is the trace operator. From the Lamé coefficients and the density the compressional (c_P) and shear (c_S) velocities of the elastic wave are obtained through the relations

$$c_P = \sqrt{(\lambda + 2\mu)/\rho}, \qquad c_S = \sqrt{\mu/\rho}. \tag{3}$$

By (formally) multiplying the first equation of (1) by a test function $\mathbf{v} \in \mathbf{V} = \mathbf{H}^1_{\Gamma_D}(\Omega) = \{\mathbf{v} \in \boldsymbol{H}^1(\Omega),\ \mathbf{v} = \mathbf{0} \text{ on } \Gamma_D\ \}$, integrating by parts over Ω and imposing the boundary conditions we obtain the following weak formulation: $\forall t \in (0, T]$ find $\mathbf{u}(t) \in \mathbf{V}$ such that

$$(\rho\ddot{\mathbf{u}}(t), \mathbf{v})_\Omega + \mathcal{A}(\mathbf{u}(t), \mathbf{v}) = \mathcal{L}(\mathbf{v}) \qquad \forall\,\mathbf{v} \in \mathbf{V}, \tag{4}$$

supplemented with the initial conditions $\mathbf{u}(0) = \mathbf{u}_0$ and $\dot{\mathbf{u}}(0) = \mathbf{v}_0$. The bilinear form $\mathcal{A}(\cdot,\cdot) : \mathbf{V}\times\mathbf{V} \to \mathbb{R}$ and the linear functional $\mathcal{L}(\cdot) : \mathbf{V} \to \mathbb{R}$ are defined as

$$\mathcal{A}(\mathbf{u}, \mathbf{v}) = (\underline{\sigma}(\mathbf{u}), \underline{\epsilon}(\mathbf{v}))_\Omega \qquad \forall\,\mathbf{u}, \mathbf{v} \in \mathbf{V}, \tag{5}$$

$$\mathcal{L}(\mathbf{v}) = (\mathbf{f}, \mathbf{v})_\Omega + (\mathbf{t}, \mathbf{v})_{\Gamma_N} \qquad \forall\,\mathbf{v} \in \mathbf{V}, \tag{6}$$

with $(\cdot,\cdot)_\Omega$ and $(\cdot,\cdot)_{\Gamma_N}$ standing for the inner product of $L^2(\Omega)$ and $L^2(\Gamma_N)$ respectively.

The following well-posedness result holds, cf. [28, Theorem 8.3-1].

Theorem 2.1. *Problem* (4) *admits a unique solution* $\mathbf{u} \in C^0((0,T];\mathbf{V}) \cap C^1((0,T];\mathbf{L}^2(\Omega))$. *provided that* $\rho \in L^\infty(\Omega)$, $\rho > 0$ *a.e. in* Ω, $\mathbf{u}_0 \in \mathbf{V}$, $\mathbf{v}_0 \in \mathbf{L}^2(\Omega)$, $\mathbf{f} \in L^2((0,T];\mathbf{L}^2(\Omega))$ *and* $\mathbf{t} \in C^1((0,T];\mathbf{H}^{\frac{1}{2}}(\Gamma_N))$.

3 Numerical discretization

In this section we introduce the finite element discretization of (4) and some technical tools that will be used in our analysis.

Mesh partitions. We consider a conforming partition $\{\mathcal{T}_h, h > 0\}$ of Ω made by open disjoint elements E such that $\overline{\Omega} = \cup_{E\in\mathcal{T}_h}\overline{E}$, with $E_i \cap E_j = \emptyset$ if $i \neq j$. The parameter h is defined as $h = \max_{E\in\mathcal{T}_h} \mathrm{diam}(E)$. We also suppose that for each element there exists an invertible map F_E defined through the relation $E = F_E(\widehat{E})$, where $\widehat{E}$ is a fixed reference element, either an hexahedron or a tetrahedron. To deal with a discontinuous approximation we define an interior face as the non-empty interior of $\partial E^+ \cap \partial E^-$, being $E^\pm$ two adjacent elements, and we define as $\mathcal{F}_h^o$ the set of all internal faces. We also assume that for any pair of elements E^+ and E^- sharing a face there exists a positive constant $\widetilde{C}$ such that $\widetilde{C}^{-1}h_{E^-} \leq h_{E^+} \leq \widetilde{C}h_{E^-}$, see [16]. Moreover, we define as $\mathcal{F}_h^D$ ($\mathcal{F}_h^N$ resp.) the set of Dirichlet (Neumann resp.) boundary faces and we collect the boundary faces in the set $\mathcal{F}_h^b = \mathcal{F}_h^D \cup \mathcal{F}_h^N$. Finally, we define $\mathcal{F}_h$ as $\mathcal{F}_h = \mathcal{F}_h^o \cup \mathcal{F}_h^b$.

For $s \geq 1$, we introduce the broken Sobolev spaces

$$\mathbf{H}^s(\mathcal{T}_h) = \left\{\mathbf{v} \in \mathbf{L}^2(\Omega) \;\; \mathbf{v}\big|_E \in \mathbf{H}^s(E) \quad \forall\, E \in \mathcal{T}_h \right\},$$
$$\mathcal{H}^s(\mathcal{T}_h) = \left\{\underline{\tau} \in \mathcal{L}^2(\Omega) \;\; \underline{\tau}\big|_E \in \mathcal{H}^s(E) \quad \forall\, E \in \mathcal{T}_h \right\}.$$

We denote by $(\cdot\,,\cdot)_{\mathcal{T}_h}$ and $\langle\cdot\,,\cdot\rangle_{\mathcal{F}_h}$ the $\mathbf{L}^2(\mathcal{T}_h) \equiv \mathbf{H}^0(\mathcal{T}_h)$ and $\mathbf{L}^2(\mathcal{F}_h) \equiv \mathbf{H}^0(\mathcal{F}_h)$ inner products, defined as

$$(\boldsymbol{\varphi},\boldsymbol{\psi})_{\mathcal{T}_h} = \sum_{E\in\mathcal{T}_h} (\boldsymbol{\varphi},\boldsymbol{\psi})_E, \quad \langle\boldsymbol{\varphi},\boldsymbol{\psi}\rangle_{\mathcal{F}_h} = \sum_{F\in\mathcal{F}_h} (\boldsymbol{\varphi},\boldsymbol{\psi})_F,$$

for any (regular enough) couple of functions $\boldsymbol{\varphi}$, $\boldsymbol{\psi}$.

Trace operators. Let E^+ and E^- be two element sharing a face $F \in \mathcal{F}_h^o$, and let $\mathbf{n}^+$ and $\mathbf{n}^-$ be the unit normal vectors to F pointing outward to E^+ and E^- respectively. For (regular enough) vector and tensor-valued functions $\mathbf{v}$ and $\underline{\tau}$ we denote by $\mathbf{v}^\pm$ and $\underline{\tau}^\pm$ the traces of $\mathbf{v}$ and $\underline{\tau}$ on F, taken within the interior of $E^\pm$, respectively. On each $F \in \mathcal{F}_h^o$, the *average* and *jump* operators are defined as

$$\begin{aligned} \{\mathbf{v}\} &= \frac{\mathbf{v}^+ + \mathbf{v}^-}{2}, & \{\underline{\tau}\} &= \frac{\underline{\tau}^+ + \underline{\tau}^-}{2}, \\ [\![\mathbf{v}]\!] &= \mathbf{v}^+ \otimes \mathbf{n}^+ + \mathbf{v}^- \otimes \mathbf{n}^-, & [\![\underline{\tau}]\!] &= \underline{\tau}^+\,\mathbf{n}^+ + \underline{\tau}^-\,\mathbf{n}^-, \end{aligned} \tag{7}$$

cf. [6]. On $F \in \mathcal{F}_h^b$, we set $\{\mathbf{v}\} = \mathbf{v}$, $\{\underline{\tau}\} = \underline{\tau}$, $[\![\mathbf{v}]\!] = \mathbf{v} \otimes \mathbf{n}$, $[\![\underline{\tau}]\!] = \underline{\tau}\mathbf{n}$.

Finite element spaces. For a given integer $N \geq 1$, we introduce the discrete space $\mathbf{V}_{DG}$ and $\mathbf{V}_{CG}$ defined as

$$\mathbf{V}_{DG} = \{\mathbf{u} \in \mathbf{L}^2(\Omega)\,, \mathbf{u} = 0 \text{ on } \Gamma_D : \; \mathbf{u}\big|_E \circ F_E \in [\mathcal{M}^N(\widehat{E})]^3 \quad \forall\, E \in \mathcal{T}_h\},$$
$$\mathbf{V}_{CG} = \{\mathbf{u} \in \mathbf{C}^0(\overline{\Omega})\,, \mathbf{u} = 0 \text{ on } \Gamma_D : \; \mathbf{u}\big|_E \circ F_E \in [\mathcal{M}^N(\widehat{E})]^3 \quad \forall\, E \in \mathcal{T}_h\},$$

where $\mathcal{M}^N(\widehat{E})$ is either the space $\mathbb{P}^N(\widehat{E})$ of polynomials of total degree at most N on $\widehat{E}$, if $\widehat{E}$ is the reference tetrahedron, or the space $\mathbb{Q}^N(\widehat{E})$ of tensor product polynomials on $\widehat{E}$ of degree N in each coordinate direction, if $\widehat{E}$ is the unit reference cube in $\mathbb{R}^3$.

3.1 Continuous and discontinuous spectral elements formulations

In the following, we introduce a family of semidiscrete approximations to problem (1). We focus on the DG discretization, since the continuous one can be seen as a special case.
The semi-discrete symmetric interior penalty DG (SIPG, see [5, 29, 8]) approximation of problem (4) reads: for a.e. $t \in (0,T]$, find $\mathbf{u} = \mathbf{u}(t) \in \mathbf{V}_{DG}$ such that

$$(\rho\ddot{\mathbf{u}}(t), \mathbf{v})_{\mathcal{T}_h} + \mathcal{A}_h(\mathbf{u}(t), \mathbf{v}) + \mathcal{B}_h(\mathbf{u}(t), \mathbf{v}) = \mathcal{L}(\mathbf{v}) \qquad \forall \mathbf{v} \in \mathbf{V}_{DG}, \tag{8}$$

where $\mathcal{L}$ is defined as in (6) and

$$\mathcal{A}_h(\mathbf{u}, \mathbf{v}) = (\underline{\sigma}(\mathbf{u}), \underline{\epsilon}(\mathbf{v}))_{\mathcal{T}_h} \qquad \forall\, \mathbf{u}, \mathbf{v} \in \mathbf{V}_{DG}, \tag{9}$$

$$\begin{aligned}\mathcal{B}_h(\mathbf{u}, \mathbf{v}) = &- \langle \{\underline{\sigma}(\mathbf{u})\}, [\![\mathbf{v}]\!] \rangle_{\mathcal{F}_h^o} - \langle [\![\mathbf{u}]\!], \{\underline{\sigma}(\mathbf{v})\} \rangle_{\mathcal{F}_h^o} \\ &+ \langle \eta_F [\![\mathbf{u}]\!], [\![\mathbf{v}]\!] \rangle_{\mathcal{F}_h^o} \qquad \forall\, \mathbf{u}, \mathbf{v} \in \mathbf{V}_{DG}\end{aligned} \tag{10}$$

On each face $F \in \mathcal{F}_h^0$ the penalty parameter η_F is defined as

$$\eta_F = \alpha \{\lambda + 2\mu\}_A N^2 / h_F, \tag{11}$$

where $\{q\}_A = 2q^+q^-/(q^+ + q^-)$ is the harmonic average of the quantity q across F, N is the polynomial degree, h_F is the area of the face F and α is a large enough positive constant to be properly chosen, see [14].

In the case of a continuous approximation the interface term $\mathcal{B}_h(\mathbf{u}, \mathbf{v})$ is identically equal to zero. Thus, the semi-discrete formulation of problem (4) can be written as: for a.e. $t \in (0,T]$, find $\mathbf{u} = \mathbf{u}(t) \in \mathbf{V}_{CG}$ such that

$$(\rho\ddot{\mathbf{u}}(t), \mathbf{v}) + \mathcal{A}(\mathbf{u}(t), \mathbf{v}) = \mathcal{L}(\mathbf{v}) \qquad \forall \mathbf{v} \in \mathbf{V}_{CG}. \tag{12}$$

Error bounds and stability estimates for problem (8) and (12) can be found in [31, 30, 2, 4].

3.2 Algebraic formulation

In this section we present the algebraic formulation stemming after space discretization with discontinuous and continuous spectral elements.
Now, let N_{dof} be the number of degrees of freedom per each component of the displacement and let $\{\mathbf{\Psi}_i^\ell\}_{i=1,...,N_{dof}}^{\ell=1,2,3}$ be a basis for the finite element space $\mathbf{V}_{DG}$ (or $\mathbf{V}_{CG}$), where $\mathbf{\Psi}_i^1 = (\psi_i, 0, 0)^T$, $\mathbf{\Psi}_i^2 = (0, \psi_i, 0)^T$ and $\mathbf{\Psi}_i^3 = (0, 0, \psi_i)^T$, for $i = 1, ..., N_{dof}$. We express a function $\mathbf{u} \in \mathbf{V}_{DG}$ (or $\mathbf{V}_{CG}$) as linear combination of the basis functions, namely

$$\mathbf{u}(\mathbf{x}, t) = \sum_{j=1}^{N_{Dof}} \begin{bmatrix} \psi_j(\mathbf{x}) \\ 0 \\ 0 \end{bmatrix} U_j^1(t) + \begin{bmatrix} 0 \\ \psi_j(\mathbf{x}) \\ 0 \end{bmatrix} U_j^2(t) \begin{bmatrix} 0 \\ 0 \\ \psi_j(\mathbf{x}) \end{bmatrix} U_j^3(t).$$

Using the above expansion and writing (8) for any test function $\mathbf{\Psi}_i^k$, $k = 1, 2, 3$, $i = 1, ..., N_{dof}$, we obtain the following second order differential system

$$\underline{M}\ddot{\mathbf{U}} + \underline{K}\mathbf{U} = \mathbf{F}, \tag{13}$$

or, blockwise,

$$\begin{bmatrix} \underline{M}^1 & 0 & 0 \\ 0 & \underline{M}^2 & 0 \\ 0 & 0 & \underline{M}^3 \end{bmatrix} \begin{bmatrix} \ddot{\mathbf{U}}^1 \\ \ddot{\mathbf{U}}^2 \\ \ddot{\mathbf{U}}^3 \end{bmatrix} + \begin{bmatrix} \underline{K}^{1,1} & \underline{K}^{1,2} & \underline{K}^{1,3} \\ \underline{K}^{2,1} & \underline{K}^{2,2} & \underline{K}^{2,3} \\ \underline{K}^{3,1} & \underline{K}^{3,2} & \underline{K}^{3,3} \end{bmatrix} \begin{bmatrix} \mathbf{U}^1 \\ \mathbf{U}^2 \\ \mathbf{U}^3 \end{bmatrix} = \begin{bmatrix} \mathbf{F}^1 \\ \mathbf{F}^2 \\ \mathbf{F}^3 \end{bmatrix}. \tag{14}$$

Each block $\underline{M}^\ell$ of the mass matrix $\underline{M}$ has the following form

$$M^\ell_{i,j} = (\rho \mathbf{\Psi}^\ell_j, \mathbf{\Psi}^\ell_i)_{\mathcal{T}_h} \qquad \ell = 1,2,3 \quad i,j = 1,...,N_{dof}.$$

The structure of the blocks M^ℓ, $\ell = 1,2,3$ clearly depends on the choice of the basis: this will be discussed later on. The entries of the stiffness matrix are given by

$$K^{\ell,m}_{i,j} = \mathcal{A}_h(\mathbf{\Psi}^m_j, \mathbf{\Psi}^\ell_i) + \mathcal{B}_h(\mathbf{\Psi}^m_j, \mathbf{\Psi}^\ell_i) \qquad \ell, m = 1,2,3, \quad i,j = 1,...,N_{dof}.$$

We recall that $\mathcal{B}_h(\cdot,\cdot) \equiv 0$ for continuous approximations. Finally, the right-hand side $\mathbf{F}$ has the following expression

$$F^\ell_i = \mathcal{L}(\mathbf{\Psi}^\ell_i), \qquad \ell = 1,2,3, \quad i,j = 1,...,N_{dof}.$$

3.3 Construction of discrete spaces

In this section we show how to choose the basis functions for the spaces $\mathbb{Q}^N(\widehat{E}_H)$ and $\mathbb{P}^N(\widehat{E}_T)$, and discuss the way this choice reflects on the structure of the linear system (14). We first discuss the case of hexahedral elements and then focus on tetrahedral elements.

3.3.1 Reference hexahedron

For the standard reference hexahedron $\widehat{E}_H = [-1,1]^3$. A basis $\{\widehat{\psi}_i\}$ of the space $\mathbb{Q}^N(\widehat{E}_H)$ is obtained by tensor product of the one dimensional nodal lagrangian functions associated with the Gauss-Legendre-Lobatto (GLL) interpolating points. On the reference element $\widehat{E}_H$ the GLL points are tensor product of the GLL points defined in the interval $[-1,1]$ that are the zeros of $(1-x^2)L'_N(x)$, where L_N is the Legendre polynomial of degree N, cfr. [7]. The dimension of the space $\mathbb{Q}^N(\widehat{E}_H)$ is thus equal to $(N+1)^3$.

The lagrangian basis functions satisfy the relation $\hat{\psi}_i(\mathbf{x}_j) = \delta_{ij}$, where δ_{ij} is the Kronecker symbol, then the components of the vector $\mathbf{U}$ in (13) represent the nodal values that the function $\mathbf{u}$ assumes at the interpolating nodes.
We recall that for spectral elements on hexahedral grids the GLL points $\{\hat{\mathbf{x}}_i\}$ are used both as quadrature points and interpolating nodes. The integral of a generic function g over an element E is then computed by

$$\int_E g(\mathbf{x})\, d\mathbf{x} = \int_{\widehat{E}_H} g(F_E(\hat{\mathbf{x}}))|J_E|\, d\hat{\mathbf{x}} \approx \sum_{i=1}^{(N+1)^3} g(F_E(\hat{\mathbf{x}}_i))|J_{F_E}|w_i, \tag{15}$$

where $|J_E|$ is the determinant of the Jacobian of the transformation F_E and w_i are the weights associated to the GLL nodes $\hat{\mathbf{x}}_i$, $i = 1,...,(N+1)^3$. This results in a diagonal structure for the mass matrix $\underline{M}$ in (13) for both discontinuous or continuous approximations.

3.3.2 Reference tetrahedron

To deal with the spectral element approximations on tetrahedral grids we consider both the reference tetrahedron $\widehat{E}_T = \{(\xi_1, \xi_2, \xi_3) : \xi_1, \xi_2, \xi_3 \geqslant -1, \xi_1+\xi_2+\xi_3 \leqslant 1\}$ and the reference hexahedron $\widehat{E}_H = \{(\eta_1, \eta_2, \eta_3) : -1 \leqslant \eta_1, \eta_2, \eta_3 \leqslant 1\}$. We introduce a transformation $T : \widehat{E}_H \to \widehat{E}_T$ (see [35]) defined as

$$\xi_1 = \frac{(1+\eta_1)(1-\eta_2)(1-\eta_3)}{4} - 1 \qquad \xi_2 = \frac{(1+\eta_2)(1-\eta_3)}{2} - 1 \qquad \xi_3 = \eta_3 \tag{16}$$

We notice that the transformation (16) maps the face $\eta_3 = 1$ of $\widehat{E}_H$ into the vertex $(-1, -1, 1)$ of $\widehat{E}_T$ and the face $\eta_2 = 1$ of $\widehat{E}_H$ to the edge $\xi_2 + \xi_3 = 0$ of $\widehat{E}_T$. For this reason the coordinate system (η_1, η_2, η_3) is often referred as the collapsed coordinate system.

The idea behind the construction of a spectral element basis on the reference tetrahedron is to exploit the tensor product structure of the collapsed coordinates to build an orthogonal basis for the space $\mathbb{P}^N(\widehat{E}_T)$, see [12, 21]. The latter, as it is, is not suitable for a C^0 approximation, but it can be modified in order to have continuous functions at the interface between elements. The basis obtained in this way is called *boundary adapted basis*, see [18, 35]. The set of boundary adapted basis functions can be split into vertex, edges, faces and interior functions. The vertex modes are defined in order to be one at the corresponding vertex and zero at in all the other vertices. The edge modes assume non zero-value along the faces sharing the edge and are zero on the remaining ones. The face modes are non-zero on the corresponding face and zero on the others. Finally, the interior modes are different from zero only inside the tetrahedron and equal to zero along the boundary. Moreover the interior modes are mutually orthogonal. We observe that, with a polynomial space of dimension N, we have four vertex modes, $N-1$ edge modes, $(N-1)(N-2)/2$ face modes and $(N-1)(N-2)(N-3)/6$ interior modes. Thus, the dimension of the space $\mathbb{P}^N(\widehat{E}_T)$ is given as expected by $(N+1)(N+2)(N+3)/6$. We report the complete expression of the basis functions in the appendix A.

The components of the vector $\mathbf{U}$, given the modal nature of the boundary adapted basis, no longer represent the nodal value of the solution $\mathbf{u}$, but they are instead the modal coefficients of its expansion with the boundary adapted basis.

The quadrature rule (15) introduced for hexahedral grids is unsuitable for spectral element approximation on tetrahedra, since the map (16) applied to GLL points causes a redundancy of quadrature points and the presence of singularities in the evaluation of shape functions derivatives (see [18]). To avoid these problems it is sufficient to use a quadrature rule that do not include the faces $\eta_2 = 1$ and $\eta_3 = 1$, as for example the Gauss-Radau or the Gauss-Legendre quadrature rule. Thus, when integrating a generic function g on a tetrahedral element, the quadrature formula reads as

$$\begin{aligned} \int_E g(\mathbf{x})\, d\mathbf{x} &= \int_{\widehat{E}_T} g(F_E(\xi_1, \xi_2, \xi_3))|J_E|\, d\boldsymbol{\xi} \\ &= \int_{\widehat{E}_H} g(F_E \circ T(\eta_1, \eta_2, \eta_3))|J_E| \frac{(1-\eta_2)}{2} \frac{(1-\eta_3)^2}{4}\, d\boldsymbol{\eta}. \end{aligned} \tag{17}$$

The term $\frac{(1-\eta_2)}{2}\frac{(1-\eta_3)^2}{2}$ is the determinant of the Jacobian $\partial(\xi_1, \xi_2, \xi_3)/\partial(\eta_1, \eta_3, \eta_3)$ and it is convenient to include its computation directly in the quadrature rule, exploiting for instance the Gauss-Jacobi quadrature rule

$$\int_{-1}^{1} (1-\eta)^\alpha (1-\eta)^\beta g(\eta)\, d\eta \approx \sum_{i=1}^{N} g(\eta_i^{\alpha,\beta}) w_i^{\alpha,\beta}, \tag{18}$$

where $\{\eta_i^{\alpha,\beta}\}$ are the zeros of the Jacobi polynomial $P_N^{\alpha,\beta}$ and $\{w_i^{\alpha,\beta}\}$ are the corresponding weights. In our case we apply (18) with $\alpha = \beta = 0$ in the η_1 direction, $\alpha = 1, \beta = 0$ in the η_2 direction, and $\alpha = 2, \beta = 0$ in the η_3 direction. Finally, (17) is numerically evaluated as

$$\int_E g(\mathbf{x})\, d\mathbf{x} \approx \sum_{p=1}^{N}\sum_{q=1}^{N}\sum_{r=1}^{N} g(F_E \circ T(\eta_{1,p}^{0,0}, \eta_{2,q}^{1,0}, \eta_{3,r}^{2,0}))|J_E| w_p^{0,0} \frac{w_q^{1,0}}{2} \frac{w_r^{2,0}}{4}.$$

3.4 Time integration scheme

In this section we briefly present the time marching scheme that is employed to integrate the second order ordinary differential system (13). We subdivide the time interval $(0, T]$ into N_T subintervals of amplitude $\Delta t = T/N_T$ and we denote by $\mathbf{U}^i$ the approximation vector $\mathbf{U}$ at time $t_i = i\Delta t$, $i = 0, ..., N_T$. To solve system (13) we apply the second order leap-frog time integration scheme. Then, at the first time step we set

$$\underline{M}\mathbf{U}^1 = (\underline{M} - \frac{\Delta t^2}{2}\underline{K})\mathbf{U}^0 - \Delta t \underline{M}\mathbf{U}^0 + \frac{\Delta t^2}{2}\mathbf{F}^0, \tag{19}$$

and at the following steps

$$\underline{M}\mathbf{U}^{n+1} = (2\underline{M} - \Delta t^2 \underline{K})\mathbf{U}^n - \underline{M}\mathbf{U}^{n-1} + \Delta t^2 \mathbf{F}^n. \qquad n = 1, ..., N_T - 1, \tag{20}$$

We notice that, on hexahedral grids the system above can be easily inverted, exploiting the structure of the mass matrix $\underline{M}$. We observe that in the case of tetrahedral grids the mass matrix is no longer diagonal, so at each time step we need to solve the linear system (20) using a suitable direct or iterative method. Here, we use a preconditioned conjugate gradient method, since $\underline{M}$ is symmetric and positive definite, see [27]. We recall that the leap-frog method is an explicit second order accurate scheme, therefore to ensure the numerical stability a CFL condition has to be satisfied, see [27]. In particular, in [4], it is shown that for the DG formulation the following condition is sufficient to ensure stability:

$$\Delta t \leqslant c^* \frac{h}{c_P N^2},$$

where $c^* = c^*(\lambda, \mu, \alpha)$ is a positive constant that depends on the Lamé coefficients and on the penalty constant α. In the case of an SIPG approximation the constant c^* is proportional to $\alpha^{-1/2}$ [4].

4 Dispersion and dissipation analysis: generalities

The aim of this section is to analyze (numerically) the dispersion and dissipation errors for the numerical schemes presented before. We recall that if the numerical wave shows a delay with respect to the physical one we have a dispersion effect, whereas if we observe a decrease in amplitude we are in presence of dissipation (cf. Fig. 1). A wave travelling in a three dimensional elastic medium can be decomposed into a pressure wave (P-wave) having velocity c_P, and a shear wave (S-wave) having velocity c_S. The P-wave induces a displacement in the same direction of the propagating wave, whereas the S-wave induces a displacement in a direction transversal to the propagating wave. Additionally, for the latter, it is possible to identify a vertical component (SV-wave), that gives a motion on a plane perpendicular to the wave direction, and a horizontal component (SH-wave), that gives a transversal motion on an horizontal plane containing the wave direction, see

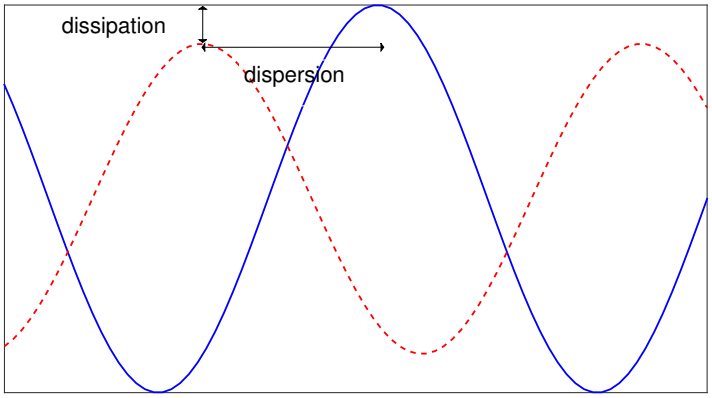

Figure 1: Example of a travelling wave (solid line) and its numerical approximation (dotted line).

[1, 34]. In the following we will measure the dispersion and the dissipation errors for both the compressional and shear velocities c_P and c_S. A standard technique to obtain quantitative estimates of these errors is the Von Neumann analysis [9, 17], that consists in propagating a plane wave of the form

$$\mathbf{u}(\mathbf{x}, t) = \mathcal{U} e^{i(\mathbf{k}\cdot\mathbf{x} - \omega t)}, \tag{21}$$

in an unbounded domain. Here, $\mathcal{U}$ represents the amplitude of the wave, ω the angular frequency and $\mathbf{k} = 2\pi/L(\cos\theta\cos\phi, \sin\theta\cos\phi, \sin\phi)$ the wave vector, being L the wavelength and θ and ϕ the angles between the direction of propagation and the coordinate axes. Obviously, the physical wave can be finally recovered by taking the real part of (21). Without loss of generality, in the following, we will assume $\mathcal{U} = 1$. Moreover, we suppose that $|\mathbf{u}(\mathbf{x}, t)| \to 0$ as $|\mathbf{x}| \to +\infty$, and absence of seismic source ($\mathbf{f} \equiv \mathbf{0}$). Under these conditions the semi-discrete problem (13) becomes

$$\underline{M}\ddot{\mathbf{U}} + \underline{K}\mathbf{U} = \mathbf{0}. \tag{22}$$

We remind that the entries of $\underline{M}$ and $\underline{K}$ have different expression, depending on whether we are employing a continuous or a discontinuous spectral elements approximation. Moreover, the components of the vector $\mathbf{U}$ can be either the nodal values of the solution for spectral elements methods on hexahedral grids or the modal expansion coefficients for spectral elements approximations on tetrahedral grids. Nevertheless, the analysis we present in the next section is carried out in a general framework and is independent of the basis adopted to span the discrete space.

In the following sections we will use a Cartesian discretization of the domain Ω into non-overlapping cubes E having uniform size h. The latter have sides parallel to the coordinate axes in order to generate a periodic tessellation of the domain. In the case of tetrahedral grids each element E is further divided into tetrahedra. We finally suppose to use the same degree of approximation N in each E.

4.1 Continuous spectral elements

To comply with unboundedness and periodicity, we consider problem (1) posed over the domain $E_{\mathcal{C}} = (-1, 1)^3$ and impose periodic boundary conditions on its boundary, con-

sisting of the faces $F_{\mathcal{R}}, F_{\mathcal{L}}, F_{\mathcal{U}}, F_{\mathcal{D}}, F_{\mathcal{F}}, F_{\mathcal{B}}$ (see Figure 2). In the case of an hexahedral grid the smallest periodic grid is made by a single element $E_{\mathcal{C}}$, whereas with tetrahedral elements it is composed by six tetrahedra (see Figure 2, right) . We consider as test and trial functions in (22) the functions $\mathbf{\Psi}_i^{\ell,E_{\mathcal{C}}}$, $\ell = 1, 2, 3$, that have support in $E_{\mathcal{C}}$. This leads to a linear system of equations of dimension $3(N+1)^3 \times 3(N+1)^3$, being N the polynomial approximation degree. In order to impose periodic boundary conditions we define J as the set of master indexes (i.e., the degrees of freedom in which we compute the solution) and with $\widehat{J}_F$, $F = \{F_{\mathcal{R}}, F_{\mathcal{U}}, F_{\mathcal{B}}\}$ the set of slave indexes (i.e., where we impose the periodicity condition). Assuming that the solution is a plane wave, we have that

$$U^{\ell}_{\widehat{j}_F} = e^{\beta_F} U^{\ell}_j \quad \ell = 1, 2, 3 \quad \forall \widehat{j}_F \in \widehat{J}_F, \tag{23}$$

where $\beta_F = \{-ik_x h, -ik_y h, -ik_z h\}$ for $F = \{F_{\mathcal{R}}, F_{\mathcal{U}}, F_{\mathcal{B}}\}$, and $\widehat{j}_F$ is the slave index in $\widehat{J}_F$ corresponding to the master index $j \in J$ on the opposite face (see for example Figure 2).

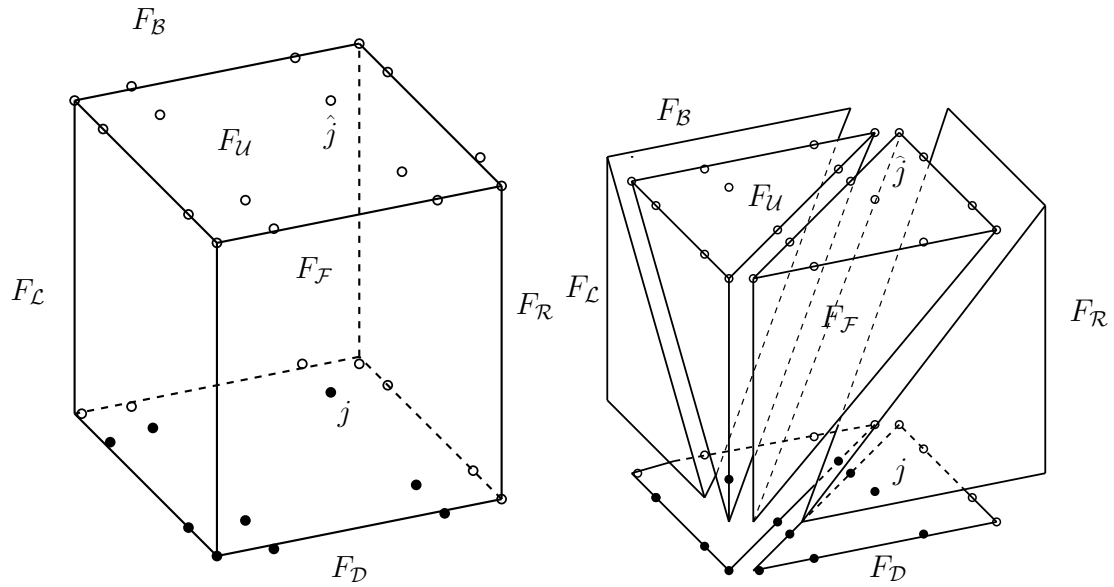

Figure 2: Periodic reference element $E_{\mathcal{C}}$ with faces $\{F_{\mathcal{U}}, F_{\mathcal{D}}, F_{\mathcal{R}}, F_{\mathcal{L}}, F_{\mathcal{F}}, F_{\mathcal{B}}\}$ and smallest pattern of periodic decomposition: hexahedral grid (left) and tetrahedral grid (right). The circles represents the degrees of freedom on top ($F_{\mathcal{U}}$) and bottom ($F_{\mathcal{D}}$) faces for a polynomial degree $N = 3$. Filled circles denote the master degrees of freedom, whereas empty circles denote the slave degrees of freedom where the periodic boundary conditions are imposed.

Imposing the periodicity conditions (23) through a suitable matrix $\Pi \in \mathbb{R}^{3(N+1)^3 \times 3N^3}$ we obtain

$$\underline{\mathcal{M}}\ddot{\mathbf{U}} + \underline{\mathcal{K}}\mathbf{U} = \mathbf{0}, \tag{24}$$

where $\underline{\mathcal{K}}$ and $\underline{\mathcal{M}}$ are given by

$$\underline{\mathcal{K}} = \Pi^T \underline{K} \Pi, \qquad \underline{\mathcal{M}} = \Pi^T \underline{M} \Pi.$$

4.2 Discontinuous spectral elements

For DGSE methods we consider the same periodicity pattern presented in the previous section. The discontinuities are imposed at the interfaces between each periodic element $E_{\mathcal{C}}$ and its neighbours (see Figure 3).

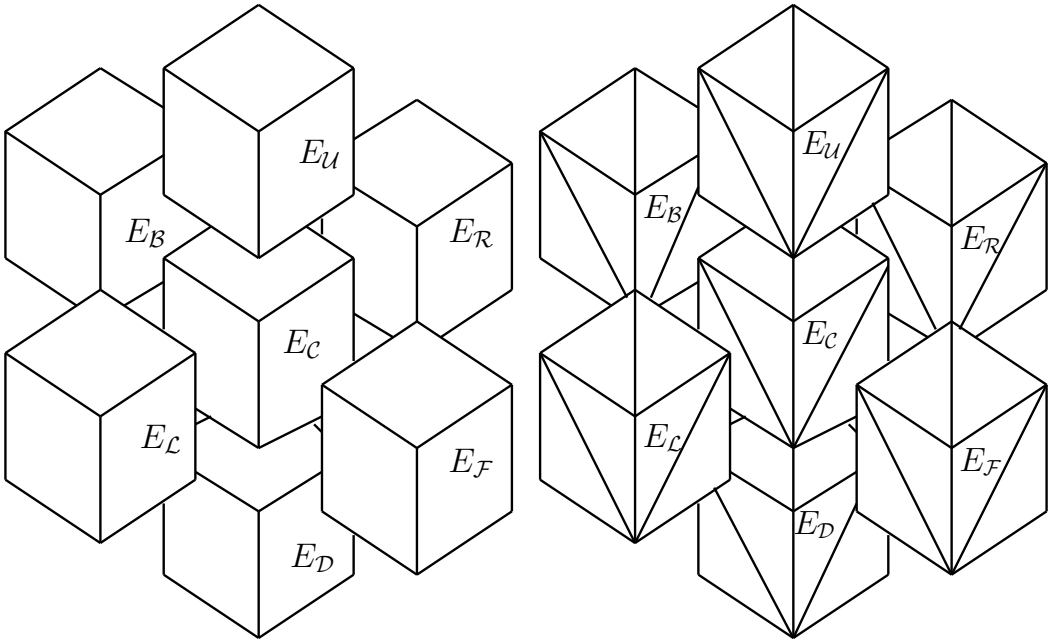

Figure 3: Periodic pattern considered in the discontinuous framework with hexahedral (left) and tetrahedral (right) elements.

Let $\mathbf{\Psi}_i^{\ell,E_f}$, $\ell = 1,2,3$, be the basis functions with support in E_f, with $f = \{\mathcal{C},\mathcal{R},\mathcal{L},\mathcal{U},\mathcal{D},\mathcal{F},\mathcal{B}\}$. Following [22], we select in (22) as test and trial functions the following

$$\mathbf{\Psi}_i^{\ell}(\mathbf{x}) = \mathbf{\Psi}_i^{\ell,E_C}(\mathbf{x}) \quad \forall \mathbf{x} \in E_{\mathcal{C}}, \tag{25}$$

$$\mathbf{\Psi}_j^{\ell}(\mathbf{x}) = \begin{cases} \mathbf{\Psi}_j^{\ell,E_{\mathcal{C}}}(\mathbf{x}) & \forall \mathbf{x} \in E_{\mathcal{C}}, \\ \mathbf{\Psi}_j^{\ell,E_f}(\mathbf{x}) & \forall \mathbf{x} \in E_f, f = \{\mathcal{R},\mathcal{L},\mathcal{U},\mathcal{D},\mathcal{F},\mathcal{B}\}, \\ 0 & \text{otherwise.} \end{cases} \tag{26}$$

This choice leads to a rectangular linear system of $21(N+1)^3$ equations in the $3(N+1)^3$ unknowns

$$\mathbf{U}^{\ell} = [\mathbf{U}^{\ell,E_{\mathcal{C}}}, \mathbf{U}^{\ell,E_{\mathcal{R}}}, \mathbf{U}^{\ell,E_{\mathcal{L}}}, \mathbf{U}^{\ell,E_{\mathcal{U}}}, \mathbf{U}^{\ell,E_{\mathcal{D}}}, \mathbf{U}^{\ell,E_{\mathcal{F}}}, \mathbf{U}^{\ell,E_{\mathcal{B}}}], \quad \ell = 1,2,3.$$

Then, the blocks in the mass and stiffness matrices in (22) become

$$\underline{M}^{\ell} = [\underline{M}^{\ell,E_{\mathcal{C}}}, \underline{0}, \underline{0}, \underline{0}, \underline{0}, \underline{0}, \underline{0}], \qquad \ell = 1,2,3, \tag{27}$$

$$\underline{K}^{\ell,m} = [\underline{A}^{\ell,m,E_{\mathcal{C}}} + \underline{B}^{\ell,m,E_{\mathcal{C}}}, \underline{B}^{\ell,m,E_{\mathcal{R}}}, \underline{B}^{\ell,m,E_{\mathcal{L}}}, \underline{B}^{\ell,m,E_{\mathcal{U}}}, \underline{B}^{\ell,m,E_{\mathcal{D}}}, \underline{B}^{\ell,m,E_{\mathcal{F}}}, \underline{B}^{\ell,m,E_{\mathcal{B}}}], \quad \ell,m = 1,2,3, \tag{28}$$

respectively, where

$$
\begin{aligned}
\underline{M}_{i,j}^{\ell,E_{\mathcal{C}}} &= \int_{E_{\mathcal{C}}} \rho \boldsymbol{\Psi}_j^{\ell,E_{\mathcal{C}}} \cdot \boldsymbol{\Psi}_i^{\ell,E_{\mathcal{C}}}, \\
\underline{A}_{i,j}^{\ell,m,E_C} &= \int_{E_C} \underline{\sigma}(\boldsymbol{\Psi}_j^{m,E_C}) : \underline{\epsilon}(\boldsymbol{\Psi}_i^{\ell,E_{\mathcal{C}}}), \\
\underline{B}_{i,j}^{\ell,m,E_{\mathcal{C}}} &= \sum_{f\in\{\mathcal{R},\mathcal{L},\mathcal{T},\mathcal{D},\mathcal{F},\mathcal{B}\}} -\int_{F_f} \{\underline{\sigma}(\boldsymbol{\Psi}_j^{m,E_{\mathcal{C}}})\} : [\![\boldsymbol{\Psi}_i^{\ell,E_{\mathcal{C}}}]\!] - \int_{F_f} [\![\boldsymbol{\Psi}_j^{m,E_{\mathcal{C}}}]\!] : \{\underline{\sigma}(\boldsymbol{\Psi}_i^{\ell,E_{\mathcal{C}}})\} \\
&\quad +\eta_f \int_{F_f} [\![\boldsymbol{\Psi}_j^{m,E_{\mathcal{C}}}]\!] : [\![\boldsymbol{\Psi}_i^{\ell,E_{\mathcal{C}}}]\!], \\
\underline{B}_{i,j}^{\ell,m,E_f} &= -\int_{F_f} \{\underline{\sigma}(\boldsymbol{\Psi}_j^{m,E_f})\} : [\![\boldsymbol{\Psi}_i^{\ell,E_{\mathcal{C}}}]\!] - \int_{F_f} [\![\boldsymbol{\Psi}_j^{m,E_f}]\!] : \{\underline{\sigma}(\boldsymbol{\Psi}_i^{\ell,E_{\mathcal{C}}})\} \\
&\quad +\eta_f \int_{F_f} [\![\boldsymbol{\Psi}_j^{m,E_f}]\!] : [\![\boldsymbol{\Psi}_i^{\ell,E_{\mathcal{C}}}]\!], \qquad f \in \{\mathcal{R},\mathcal{L},\mathcal{T},\mathcal{D},\mathcal{F},\mathcal{B}\}.
\end{aligned}
$$

In order to obtain a square linear system we use (21), i.e. the expression of the plane wave, $\mathbf{u}(\mathbf{x},t) = e^{i(\mathbf{k}\cdot\mathbf{x}-\omega t)}$, and this, together with the imposition periodic conditions, implies that

$$
U_j^{\ell,E_f} = e^{\beta_f} U_j^{\ell,E_{\mathcal{C}}}, \qquad \ell = 1,2,3, \tag{29}
$$

where $\beta_f = \{-ik_xh, ik_xh, -ik_zh, ik_zh, ik_yh, -ik_yh\}$ for $f = \{\mathcal{R},\mathcal{L},\mathcal{U},\mathcal{D},\mathcal{F},\mathcal{B}\}$, respectively. Substituting (29) in (27) and (28) leads to the following linear system of $3(N+1)^3$ equations in $3(N+1)^3$ unknowns $\mathbf{U} = \mathbf{U}^{E_{\mathcal{C}}}$

$$
\underline{M}\ddot{\mathbf{U}} + \underline{\widetilde{K}}\mathbf{U} = \mathbf{0}. \tag{30}
$$

The components of the matrix $\underline{\tilde{K}}$ are defined as

$$
\underline{\widetilde{K}}^{\ell,m} = \underline{A}^{\ell,m,E_{\mathcal{C}}} + \underline{B}^{\ell,m,E_{\mathcal{C}}} + \sum_{f\in\{\mathcal{R},\mathcal{L},\mathcal{U},\mathcal{D},\mathcal{F},\mathcal{B}\}} e^{\beta_f} \underline{B}^{\ell,m,E_f}, \qquad \ell,m = 1,2,3.
$$

5 Semi-discrete formulation: dispersion and dissipation analysis

In this section we analyse the dispersion and dissipation properties, assuming exact time integration. Taking the second derivative with respect to time in (24) and (30) we find the generalized eigenvalue problems

$$
\underline{\mathcal{K}}\mathbf{U} = \omega^2 \underline{\mathcal{M}}\mathbf{U}, \tag{31}
$$

$$
\underline{\widetilde{K}}\mathbf{U} = \omega^2 \underline{M}\mathbf{U}. \tag{32}
$$

5.1 Dispersion analysis

By solving numerically (31) and (32) we obtain the eigenvalues $\xi = \omega_h^2$ that represent the best approximations of the angular frequencies of the travelling waves. For a 3D plane wave we can distinguish between the frequency ω_P, which is related to the longitudinal displacement, and the two frequencies $\omega_{SV} = \omega_{SH}$, which are related to the transversal displacement of vertically polarized (SV) and horizontally polarised (SH) shear waves, respectively. The number of eigenvalues obtained through (31) and (30), in general, exceeds

the number of physical modes. Then, we identify the numerical eigenvalues ξ_P and ξ_S, corresponding to the physical frequencies, by computing the numerical velocities obtained for each eigenvalue and comparing them to the real values of c_P and c_S. We remark that the computed eigenvalues approximating ω_{SV} and ω_{SH} are not exactly the same but their difference is negligible [32, 37]. In the following we will select ξ_S as that eigenvalue, between the two physically relevant, that leads to the worst approximation of c_S.

Once selected the eigenvalues ξ_P and ξ_S, we compute the numerical angular frequencies $\omega_{P,h} = \sqrt{\xi_P}$ and $\omega_{S,h} = \sqrt{\xi_S}$ for P-wave and S-wave, respectively. The numerical wave velocities are therefore given by

$$c_{P,h} = \frac{h\,\omega_{P,h}}{2\pi\delta}, \qquad c_{S,h} = \frac{h\,\omega_{S,h}}{2\pi\delta},$$

where $\delta = h/(NL)$ is the sampling ratio, i.e. the number of interpolation points per wavelength, and L is the wavelength. In the following we consider the relative dispersion errors

$$e_P = \frac{c_{P,h}}{c_P} - 1, \qquad e_S = \frac{c_{S,h}}{c_S} - 1.$$

Note that e_P, $e_S > 0$ implies that the numerical wave propagates faster than the physical ones.

Numerical results

We now investigate how the dispersion error depends on the polynomial degree N, the sampling ratio δ and the angles of incidence θ and ϕ of the plane wave. In the following tests we fix the mechanical parameters $\rho = 2$, $\lambda = 1$ and $\mu = 0.5$, and the wave velocities $c_P = 1$ and $c_S = 0.5$, with a ratio $r = c_P/c_S = 2$. Notice that a ratio $r \simeq 2$ is a realistic value in geophysical applications. In all tests performed with the DGSE approximation we set the value of the penalty constant $\alpha = 10$. For the first case, we consider $\delta = 0.2$, i.e., five nodes per wavelength, and we set the incidence angles $\phi = \theta = \pi/4$. In Figure 4 we observe an exponential decay of the dispersion error with respect to the polynomial degree N, using both continuous and discontinuous approximations on hexahedral and tetrahedral grids.

In Figure 5, we report the computed grid dispersion error as a function of δ for different approximation degrees $N = 2, 3, 4$. Looking at the slopes of the e_P and e_S curves we get the following empirical estimate of the orders of convergence, i.e., $e_P = \mathcal{O}(h^{2N})$ and $e_S = \mathcal{O}(h^{2N})$ respectively.

Finally, we study the dispersion error as a function of the angles of incidence of the plane wave. In Figure 6 we report the results obtained with DGSE discretization. An analogous behaviour is observed for continuous approximations. We set the polynomial degree $N = 3$ and the sampling ratio $\delta = 0.2$. We notice that with hexahedral grids the error behaves symmetrically with respect to the origin of the axes, whereas with tetrahedral grids the error grows along the direction in which the periodic cell E_C is cut into tetrahedra.

We also observe that, fixing a threshold for the grid dispersion errors, SE on hexahedral elements perform better than those on tetrahedral ones. However, for the latter, low dispersion errors (less than 10^{-6}) can be obtained choosing a suitable value for the polynomial degree of interpolation and for the number of points per wavelength, for instance $N > 4$ and $\delta \leq 0.2$, see Figures 4 and 5. Moreover, with both kinds of elements, the use of a discontinuous approximation does not introduce significant changes with respect to the continuous one.

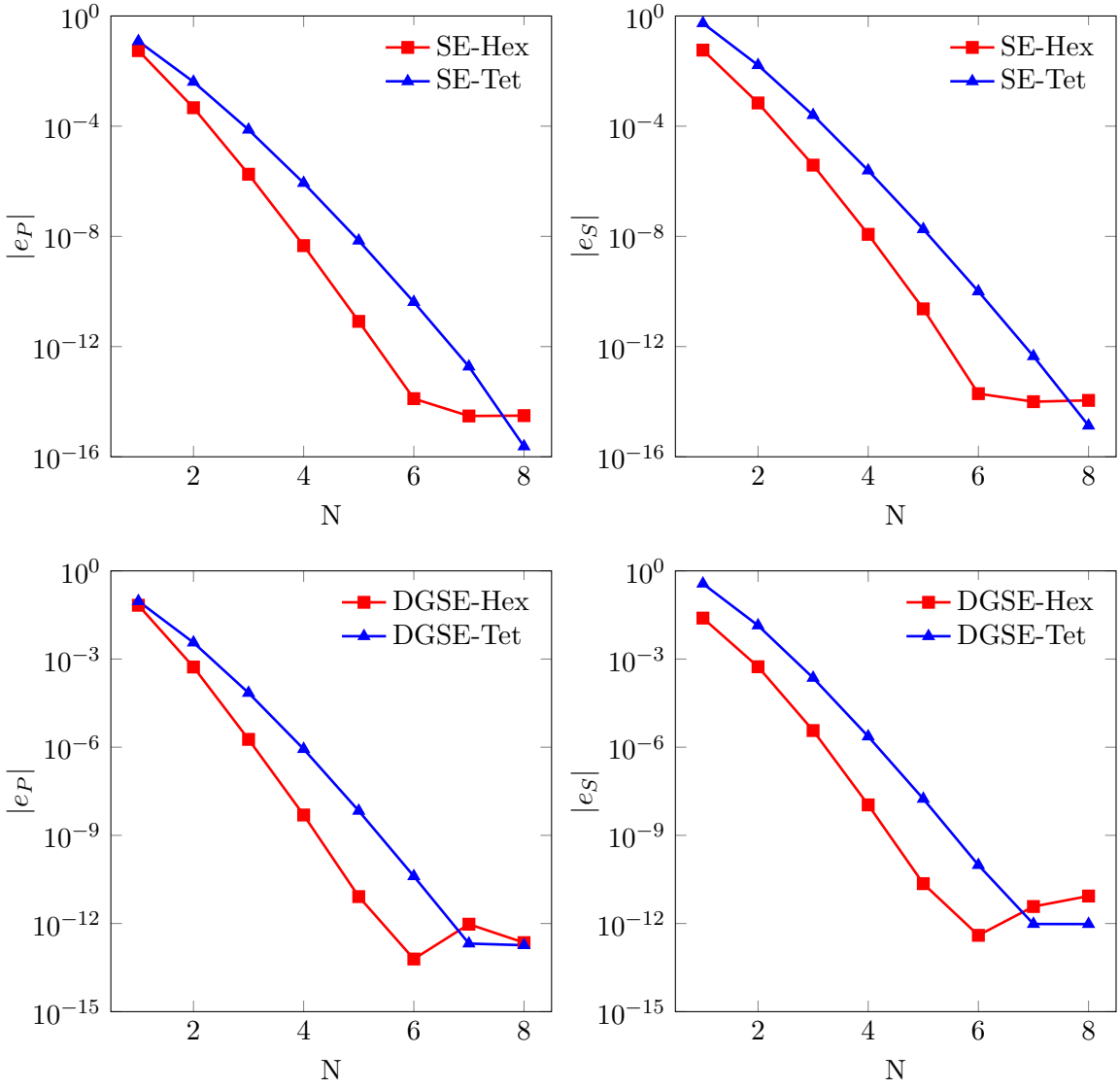

Figure 4: Dispersion errors $|e_P|$ and $|e_S|$ versus N with $\delta = 0.2$ and $\theta = \varphi = \pi/4$. Continuous spectral elements (SE, top) and discontinuous spectral elements (DGSE, bottom) on both hexahedral (Hex) and tetrahedral (Tet) grids.

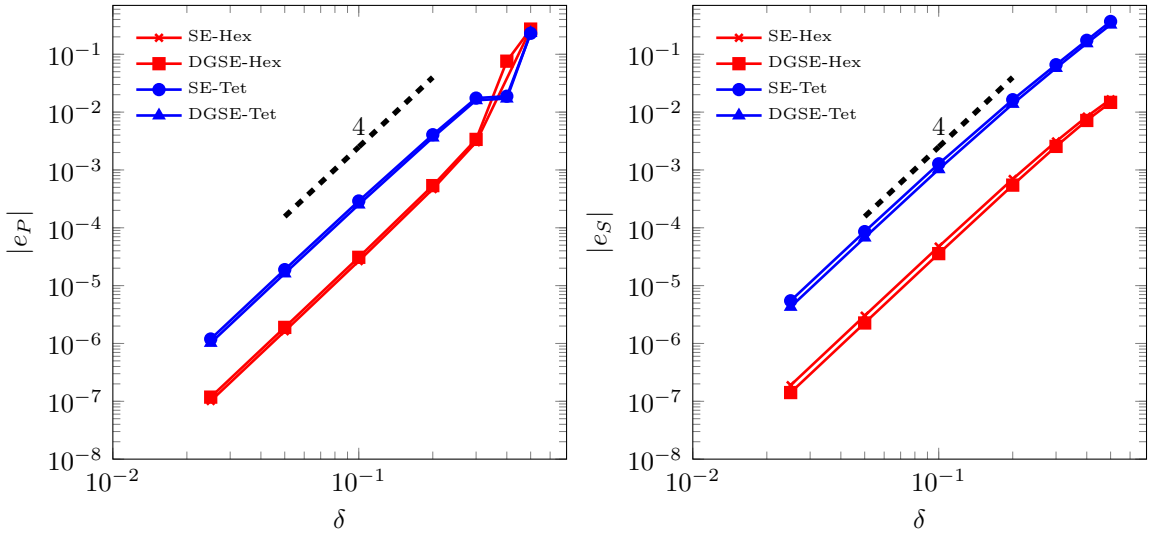

(a) $N = 2$

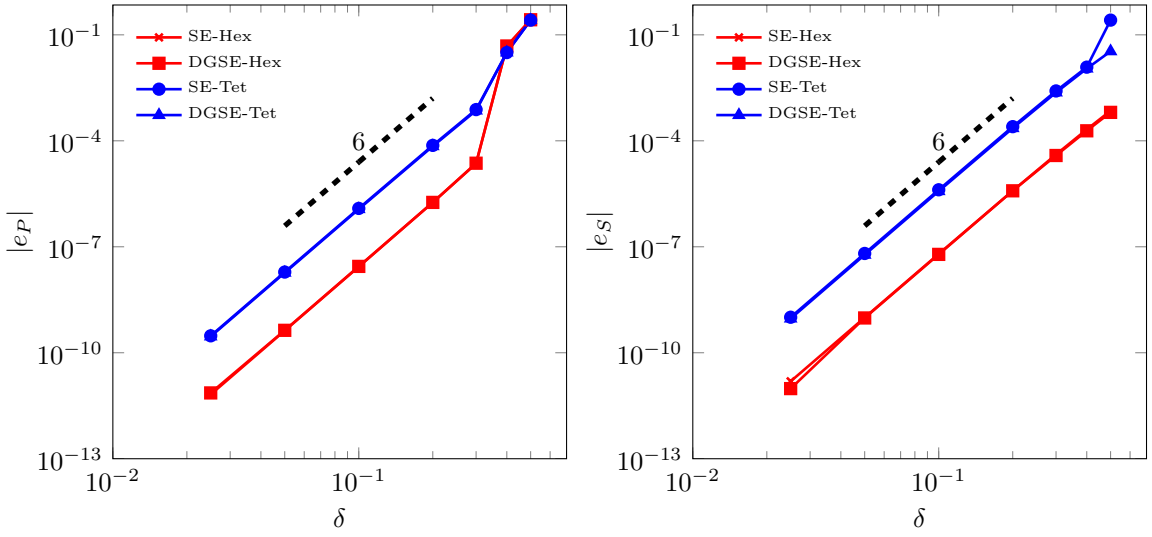

(b) $N = 3$

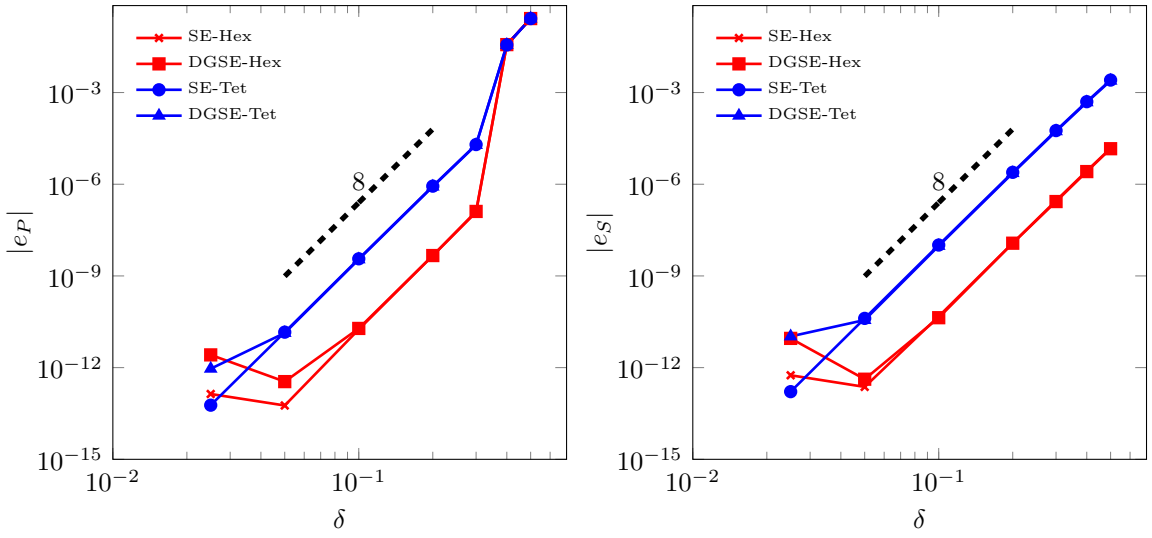

(c) $N = 4$

Figure 5: Dispersion errors versus δ for $N = 2, 3, 4$, for continuous spectral elements (SE) and discontinuous spectral elements (DGSE) on both hexahedral (Hex) and tetrahedral (Tet) grids.

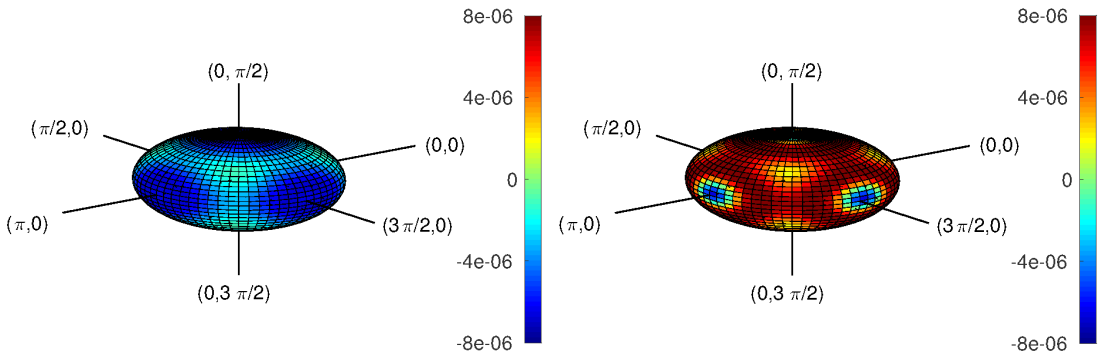

(a) e_P,hexahedral grid

(b) e_S,hexahedral grid

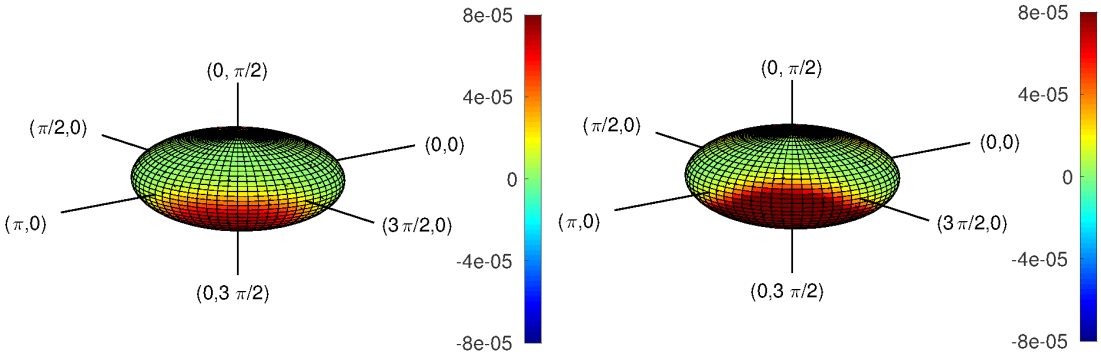

(c) e_P,tetrahedral grid

(d) e_S,tetrahedral grid

Figure 6: Dispersion errors e_P (left) and e_S (right) as a function of the incidence angles (θ, ϕ). DG spectral elements approximation on hexahedral (top) and tetrahedral (bottom) grids.

5.2 Dissipation analysis

For the dissipation error we study the amplitude of the numerical displacement. Considering as exact solution of (22) the unitary amplitude plane wave, we can express its amplitude as

$$|e^{i(\mathbf{k}\cdot\mathbf{x}-\omega t)}| = e^{tIm(\omega)}.$$

Since the physical wave satisfies $Im(\omega) = 0$, its amplitude is equal to 1 for all times t. On the contrary, the numerical wave will have in general $Im(\omega_h) \neq 0$. Then, we say that the scheme is non dissipative if $Im(\omega_h) = 0$, whereas it is dissipative if $Im(\omega_h) < 0$. To give a quantitative estimate of the dissipation errors, we will compute $Im(\omega_{P,h})$ and $Im(\omega_{S,h})$.

Numerical results

In Tables 1 and 2 we report the values of dissipation errors for different values of the polynomial degree and the sampling ratio. The results reported refer only to the continuous case. Numerical tests performed with discontinuous approximations display similar values. Since these values are all near machine precision we can state that the analysed schemes do not suffer from dissipation errors.

	SE-Hex		SE-Tet	
N	$Im(\omega_{P,h})$	$Im(\omega_{S,h})$	$Im(\omega_{P,h})$	$Im(\omega_{S,h})$
2	-4.124e-16	-5.534e-16	1.712e-17	1.468e-17
4	-3.913e-16	7.401e-15	-2.078e-16	1.339e-16
6	-4.259e-18	1.556e-16	-1.504e-17	-2.065e-16

Table 1: Dissipation error for $N = 2, 4, 6$ and $\delta = 0.2$ for continuous spectral elements (SE) on both hexahedral (Hex) and tetrahedral (Tet) grids.

	SE-Hex		SE-Tet	
δ	$Im(\omega_{P,h})$	$Im(\omega_{S,h})$	$Im(\omega_{P,h})$	$Im(\omega_{S,h})$
0.4	-2.041e-17	3.228e-17	1.016e-16	-6.736e-16
0.2	-3.913e-16	7.401e-15	-2.078e-16	1.339e-16
0.1	-2.076e-16	1.011e-16	1.297e-17	-7.022e-17
0.05	-3.432e-17	1.073e-16	-2.547e-17	-5.996e-17

Table 2: Dissipation error for $\delta = 0.4, 0.2, 0.1, 0.05$, $N = 4$, for continuous spectral elements (SE) on both hexahedral (Hex) and tetrahedral (Tet) grids.

6 Fully-discrete formulation: dispersion and dissipation analysis

In this section we investigate dispersion and dissipation behaviours of the solution of the fully-discrete problem when the leap-frog time integration scheme is applied to the semi-discrete problem (22). The latter is a typical choice for time integration in the framework of computational seismology, see for instance [9, 15, 20]. Substituting (21) with $\mathcal{U} = 1$

into (24) we obtain

$$\underline{\mathcal{M}}(e^{-i\omega t_{j+1}} - 2e^{-i\omega t_j} + e^{-i\omega t_{j-1}})\frac{\mathbf{U}_0}{\Delta t^2} + \underline{\mathcal{K}}e^{-i\omega t_j}\mathbf{U}_0 = \mathbf{0}, \quad j = 1, ..., N_T - 1. \tag{33}$$

The above system can be rewritten as

$$\underline{\mathcal{M}}(2 - e^{-i\omega\Delta t} - e^{i\omega\Delta t})\frac{\mathbf{U}_0}{\Delta t^2} = \underline{\mathcal{K}}\mathbf{U}_0.$$

Now, using the following relation

$$2 - e^{-i\omega\Delta t} - e^{i\omega\Delta t} = 2(\cos(\omega\Delta t) - 1) = 4\sin^2\left(\omega\frac{\Delta t}{2}\right),$$

we obtain a generalized eigenvalues problem of the form

$$\underline{\mathcal{K}}\mathbf{U}_0 = \Lambda\underline{\mathcal{M}}\mathbf{U}_0,$$

where the eigenvalues Λ are related to the angular frequency of the grid ω_h through the relation

$$\Lambda = \frac{4}{\Delta t^2}\sin^2(\omega_h\frac{\Delta t}{2}), \qquad \omega_h = \frac{2}{\Delta t}\arcsin(\frac{\Delta t}{2}\sqrt{\Lambda}).$$

The same result can be obtained by applying the leap-frog method to (30).
Now the dispersion and the dissipation errors can be computed as described in Section 5.

Numerical results

We present the grid dispersion and dissipation errors for the fully discrete approximation, varying both the parameters N, δ, θ, ϕ and the time step Δt. In the following, for brevity, we will present only the results related to the DGSE discretization. Similar results can be obtained with the continuous approach.

We first address the behaviour of the dispersion error by varying the polynomial degree N. In particular, we compute the dispersion errors versus N for different time steps Δt, fixing the values of velocities, sampling ratio and incident angles as $c_P = 1$, $c_S = 0.5$, $\delta = 0.2$ and $\phi = \theta = \pi/4$. In Figure 7 we observe that as Δt goes to zero we retrieve the exponential convergence as already observed in the semi-discrete case. Indeed, for sufficiently small values of Δt, the following asymptotic relation holds

$$\omega_h \approx \sqrt{\Lambda} + \mathcal{O}(\Delta t^2),$$

see [3]. Thus ω_h decays as in the semi-discrete case until the term Δt^2 becomes dominant. In Figure 8 we compare the behaviour of the fully discrete scheme obtained on both hexahedral and tetrahedral grids using $\Delta t = 0.001$. We notice that the same level of accuracy is obtained with both grids for a polynomial degree $N \geq 5$.

Next, we analyse the dispersion error with respect to the sampling ratio δ, using $N = 4$. As Δt approaches zero, the fully-discrete curves recover the semi-discrete ones (see Figure 9). In Figure 10 we compare the results obtained with both hexahedral and tetrahedral elements with a time step $\Delta t = 0.001$. We observe that for $\delta \leq 0.1$, i.e., ten points per wavelength, both methods retain the same level of accuracy.

Finally, in Table 3 and 4 we report the computed values of the dissipation errors with a fixed value $\Delta t = 0.001$, varying the polynomial degree N and the sampling ratio δ, respectively. The results obtained show that dissipative behaviours are negligible also for the fully-discrete formulation, as expected from the results obtained in [22, 3].

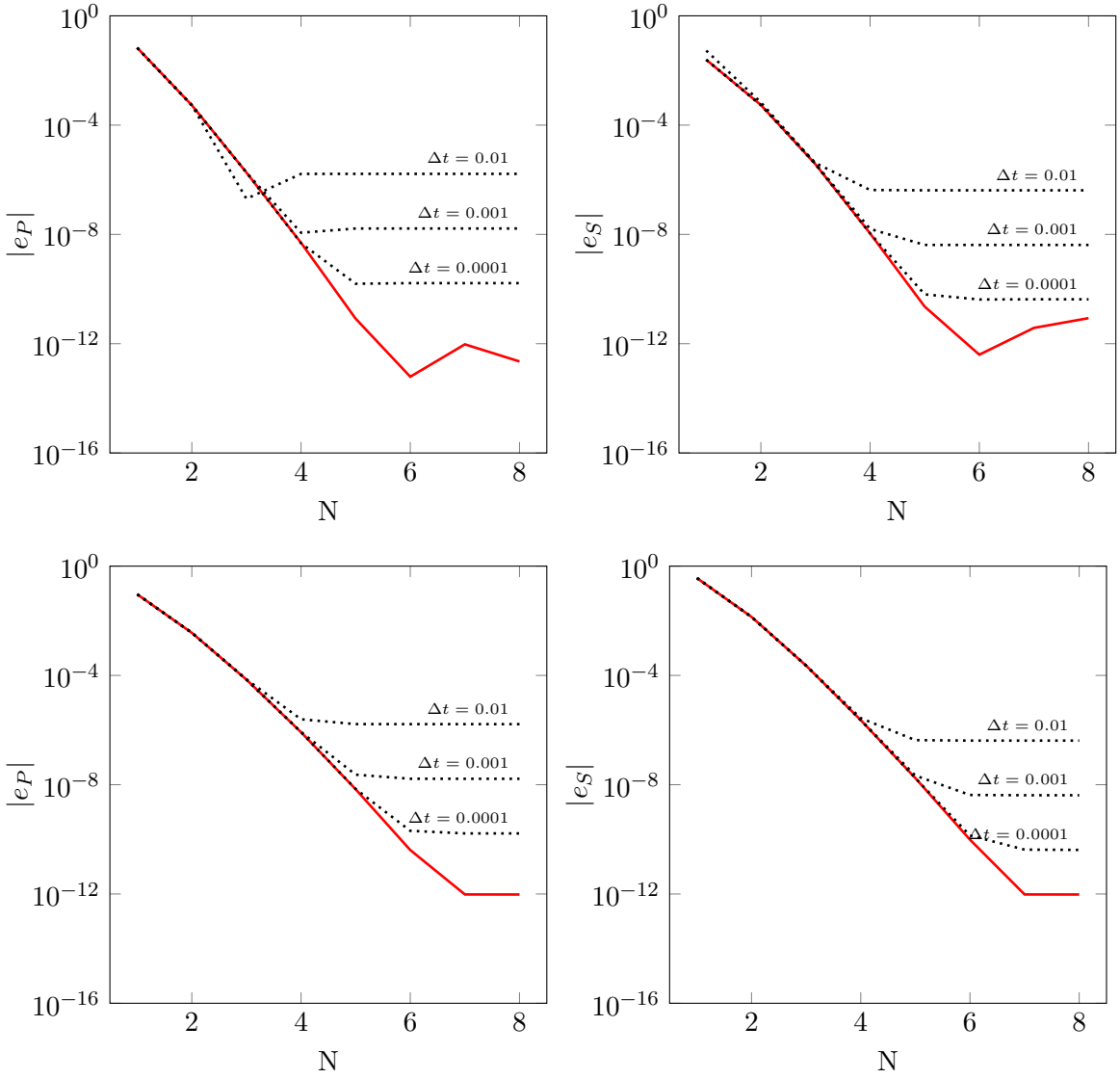

Figure 7: Dispersion errors e_P (left) and e_S (right) as a function of N, using discontinuous spectral elements on both hexahedral (top) and tetrahedral (bottom) grids. The continuous lines refers to the semi-discrete approximation, the dotted lines refers to the fully discrete approximation with $\Delta t = 0.01, 0.001, 0.0001$.

	DGSE-Hex		DGSE-Tet	
N	$Im(\omega_{P,h})$	$Im(\omega_{S,h})$	$Im(\omega_{P,h})$	$Im(\omega_{S,h})$
2	-1.070e-15	5.094-15	-1.595e-15	6.839e-16
4	-7.548e-15	1.876e-14	-9.681-15	3.392e-14
6	3.044e-15	4.390e-14	-8.898e-14	-6.686e-14

Table 3: Dissipation errors for P- and S-waves: $N = 2, 4, 6$, $\delta = 0.2$ and $\Delta t = 0.001$. Discontinuous spectral elements (DGSE) on both hexahedral (Hex) and tetrahedral (Tet) elements.

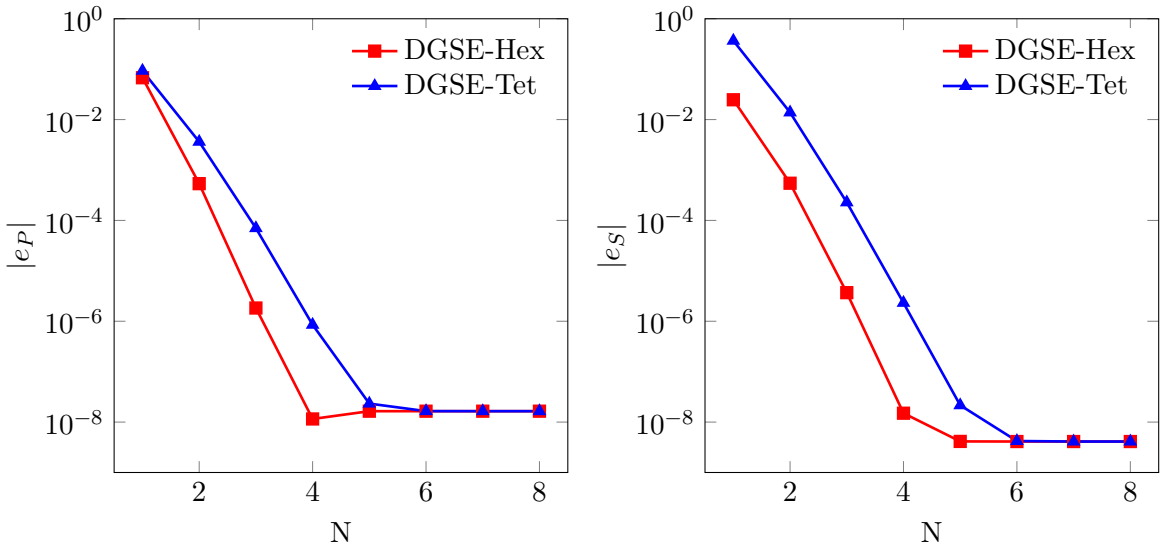

Figure 8: Dispersion errors e_P (left) and e_S (right) as a function of N with a time step $\Delta t = 0.001$, using discontinuous spectral elements (DGSE) on both hexahedral (Hex) and tetrahedral (Tet) grids.

	DGSE-Hex		DGSE-Tet	
δ	$Im(\omega_{P,h})$	$Im(\omega_{S,h})$	$Im(\omega_{P,h})$	$Im(\omega_{S,h})$
0.4	-1.745e-15	-6.608e-15	6.423e-13	5.115e-14
0.2	-7.549e-15	2.351e-14	-9.681-15	3.392e-14
0.1	-2.584e-14	2.063e-14	9.7423e-15	-5.749e-14
0.05	-2.664e-14	3.515e-15	-2.233e-15	-4.311e-14

Table 4: Dissipation errors for P- and S-waves for $\delta = 0.4, 0.2, 0.1, 0.05$, $N = 4$ and $\Delta t = 0.001$. Discontinuous spectral elements (DGSE) on both hexahedral (Hex) and tetrahedral (Tet) elements.

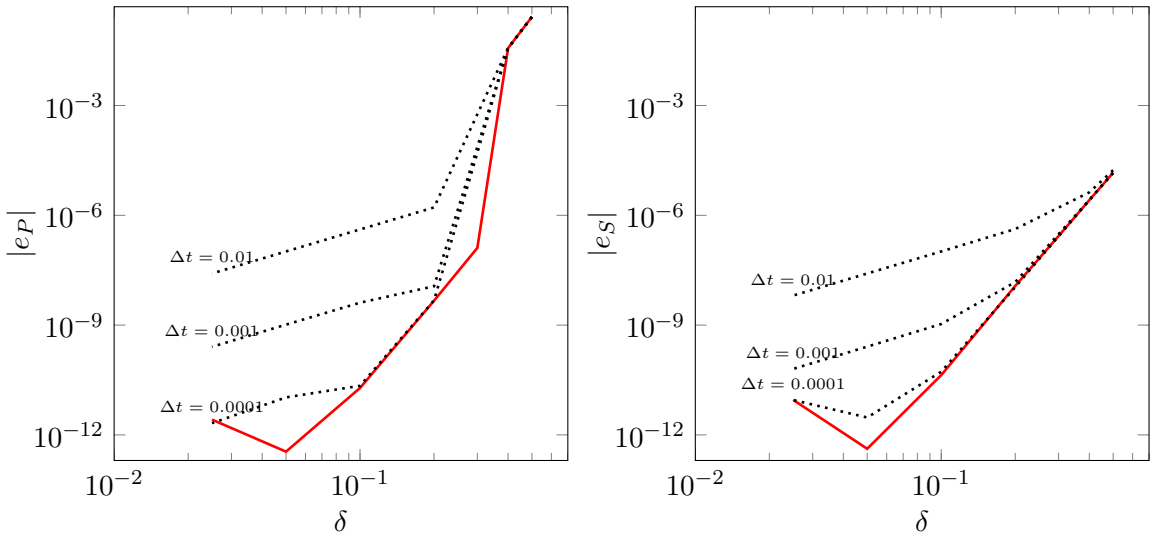

(a) DGSE-Hex

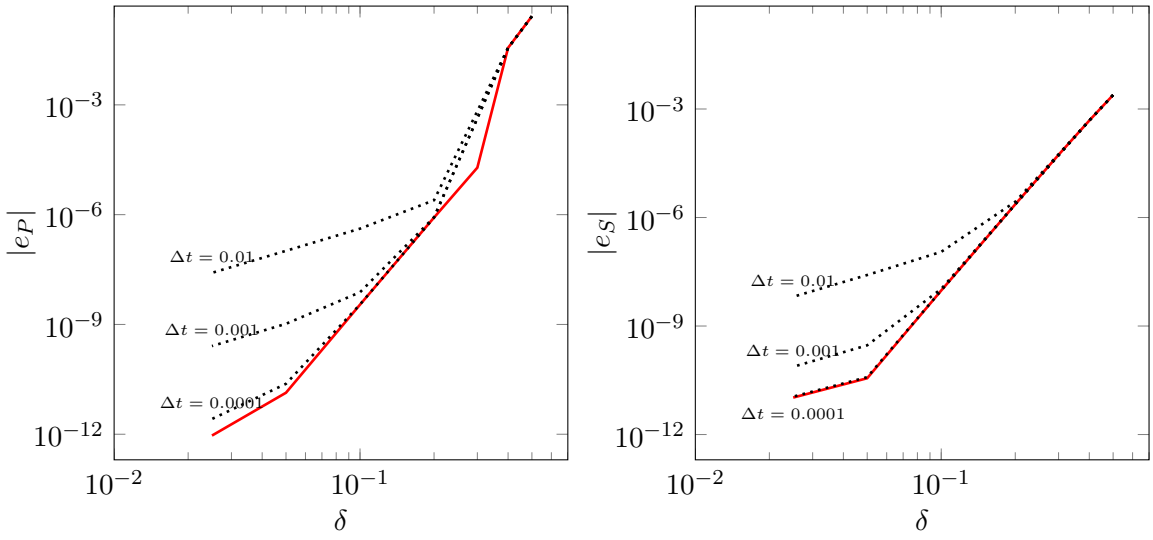

(b) DGSE-Tet

Figure 9: Dispersion errors for P- and S-waves as a function of δ using discontinuous spectral elements (DGSE) on hexahedral (Hex) and tetrahedral (Tet) grids, with a fixed polynomial degree $N = 4$. The continuous lines refers to the semi-discrete approximation, the dotted lines refers to the fully discrete approximation with $\Delta t = 0.01, 0.001, 0.0001$.

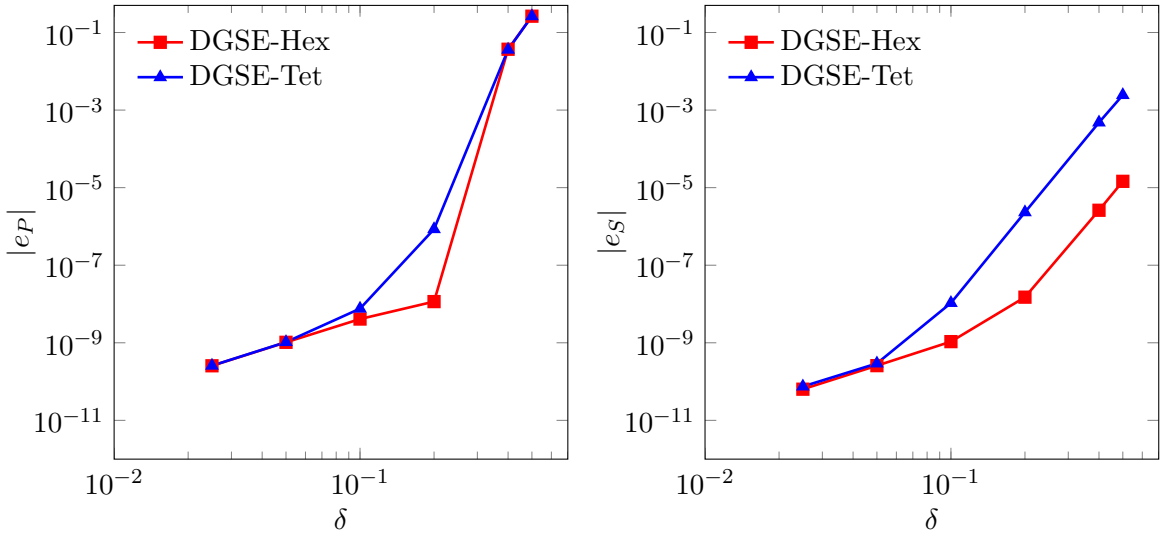

Figure 10: Dispersion errors e_P (left) and e_S (right) versus δ, fixing $N = 4$ and $\Delta t = 0.001$. Discontinuous spectral elements (DGSE) on both hexahedral (Hex) and tetrahedral (Tet) grids.

7 Conclusions

In this paper we have presented a comprehensive dispersion and dissipation numerical analysis for three dimensional elastic wave propagation problems discretized using (both discontinuous and continuous) spectral element methods on both hexahedral and tetrahedral grids. Our analysis has been applied to the semi-discrete and the fully-discrete formulation, the latter obtained using the leap-frog time integration scheme. The results obtained show that all the considered techniques retain low dispersion and dissipation errors. In particular, we can conclude that :

- for both continuous and discontinuous spectral element methods the computed dispersion errors on hexahedral meshes are much lower than the corresponding ones computed on tetrahedral meshes;

- both continuous and discontinuous spectral element methods show negligible dispersion errors (i.e., less than 10^{-6}),provided that a polynomial degree $N \geq 4$ and more than 5 (10 resp.) points per wavelength are employed on hexahedral (tetrahedral resp.) grids;

- the leap-frog time integration scheme does not introduce any further significant dispersion and dissipation errors to those arising from space discretization. Indeed, the error curves follow the ones obtained in the semi-discrete case until the time discretization error becomes dominant.

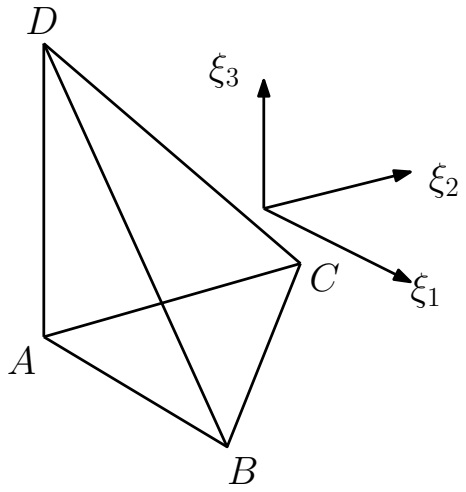

Figure 11: Reference tetrahedron

A Basis functions for tetrahedral elements

We consider the reference tetrahedron $\widehat{E}_T$ and the collapsed reference system (η_1, η_2, η_3) as defined in Section 3. Identifying with A, B, C and D the vertices $(-1,-1,-1)$, $(-1,1,-1)$, $(1,-1,-1)$ and $(-1,-1,1)$ (see Figure 11), respectively, the basis functions for the space $\mathbb{P}^{\mathbb{N}}(\widehat{E}_T)$ have the following form

$$\text{Vertex A} : \left(\frac{1-\eta_1}{2}\right)\left(\frac{1-\eta_2}{2}\right)\left(\frac{1-\eta_3}{2}\right),$$

$$\text{Vertex B} : \left(\frac{1+\eta_1}{2}\right)\left(\frac{1-\eta_2}{2}\right)\left(\frac{1-\eta_3}{2}\right),$$

$$\text{Vertex C} : \left(\frac{1+\eta_2}{2}\right)\left(\frac{1-\eta_3}{2}\right),$$

$$\text{Vertex D} : \left(\frac{1+\eta_3}{2}\right),$$

$$\text{Edge AB} : \left(\frac{1-\eta_1}{2}\right)\left(\frac{1+\eta_1}{2}\right) P_{p-1}^{1,1}(\eta_1) \left(\frac{1-\eta_2}{2}\right)^{p+1} \left(\frac{1-\eta_3}{2}\right)^{p+1}, \qquad 0 < p < N,$$

$$\text{Edge AC} : \left(\frac{1-\eta_1}{2}\right)\left(\frac{1-\eta_2}{2}\right)\left(\frac{1+\eta_2}{2}\right) P_{p-1}^{1,1}(\eta_2) \left(\frac{1-\eta_3}{2}\right)^{p+1}, \qquad 0 < p < N,$$

$$\text{Edge BC} : \left(\frac{1+\eta_1}{2}\right)\left(\frac{1-\eta_2}{2}\right)\left(\frac{1+\eta_2}{2}\right) P_{p-1}^{1,1}(\eta_2) \left(\frac{1-\eta_3}{2}\right)^{p+1}, \qquad 0 < p < N,$$

$$\text{Edge AD} : \left(\frac{1-\eta_1}{2}\right)\left(\frac{1-\eta_2}{2}\right)\left(\frac{1-\eta_3}{2}\right)\left(\frac{1+\eta_3}{2}\right) P_{p-1}^{1,1}(\eta_3), \qquad 0 < p < N,$$

$$\text{Edge BD} : \left(\frac{1+\eta_1}{2}\right)\left(\frac{1-\eta_2}{2}\right)\left(\frac{1-\eta_3}{2}\right)\left(\frac{1+\eta_3}{2}\right) P_{p-1}^{1,1}(\eta_3), \qquad 0 < p < N,$$

$$\text{Edge CD} : \left(\frac{1+\eta_2}{2}\right)\left(\frac{1-\eta_3}{2}\right)\left(\frac{1+\eta_3}{2}\right) P_{p-1}^{1,1}(\eta_3), \qquad 0 < p < N,$$

$$\text{Face ABC}: \left(\frac{1-\eta_1}{2}\right)\left(\frac{1+\eta_1}{2}\right)P_{p-1}^{1,1}(\eta_1)\left(\frac{1-\eta_2}{2}\right)^{p+1}\left(\frac{1+\eta_2}{2}\right)$$
$$P_{q-1}^{2p+1,1}(\eta_2)\left(\frac{1-\eta_3}{2}\right)^{p+q+1}, \qquad 0<p,q,p+q<N,$$

$$\text{Face ABD}: \left(\frac{1-\eta_1}{2}\right)\left(\frac{1+\eta_1}{2}\right)P_{p-1}^{1,1}(\eta_1)\left(\frac{1-\eta_2}{2}\right)^{p+1}\left(\frac{1-\eta_3}{2}\right)^{p+1}$$
$$P_{q-1}^{2p+1,1}(\eta_3)\left(\frac{1+\eta_3}{2}\right), \qquad 0<p,q,p+q<N,$$

$$\text{Face ACD}: \left(\frac{1-\eta_1}{2}\right)\left(\frac{1-\eta_2}{2}\right)\left(\frac{1+\eta_2}{2}\right)P_{p-1}^{1,1}(\eta_2)\left(\frac{1-\eta_3}{2}\right)^{p+1}$$
$$P_{q-1}^{2p+1,1}(\eta_3)\left(\frac{1+\eta_3}{2}\right), \qquad 0<p,q,p+q<N,$$

$$\text{Face BCD}: \left(\frac{1+\eta_1}{2}\right)\left(\frac{1-\eta_2}{2}\right)\left(\frac{1+\eta_2}{2}\right)P_{p-1}^{1,1}(\eta_2)\left(\frac{1-\eta_3}{2}\right)^{p+1}$$
$$P_{q-1}^{2p+1,1}(\eta_3)\left(\frac{1+\eta_3}{2}\right), \qquad 0<p,q,p+q<N,$$

$$\text{Interior}: \left(\frac{1-\eta_1}{2}\right)\left(\frac{1+\eta_1}{2}\right)P_{p-1}^{1,1}(\eta_1)\left(\frac{1-\eta_2}{2}\right)^{p+1}\left(\frac{1+\eta_2}{2}\right)$$
$$P_{q-1}^{2p+1,1}(\eta_2)\left(\frac{1-\eta_3}{2}\right)^{p+q+1}\left(\frac{1+\eta_3}{2}\right)P_{r-1}^{2p+2q+1,1}, \qquad 0<p,q,r,p+q+r<N,$$

where $P_p^{\alpha,\beta}$ is the Jacobi polynomial of degree p and parameter α and β, see [18].

References

[1] K. Aki and P. G. Richards. *Quantitative seismology*, volume 1. Sausalito, CA: University Science Books, 2002.

[2] P. F. Antonietti, B. A. de Dios, I. Mazzieri, and A. Quarteroni. Stability analysis of discontinuous galerkin approximations to the elastodynamics problem. *Journal of Scientific Computing*, pages 1–28, 2015.

[3] P. F. Antonietti, C. Marcati, I. Mazzieri, and A. Quarteroni. High order discontinuous Galerkin methods on simplicial elements for the elastodynamics equation. *Numerical Algorithms*, pages 1–26, 2015.

[4] P. F. Antonietti, I. Mazzieri, A. Quarteroni, and F. Rapetti. Non-conforming high order approximations of the elastodynamics equation. *Computer Methods in Applied Mechanics and Engineering*, 209:212–238, 2012.

[5] D. N. Arnold. An interior penalty finite element method with discontinuous elements. *SIAM Journal on Numerical Analysis*, 19(4):742–760, 1982.

[6] D. N. Arnold, F. Brezzi, B. Cockburn, and L. D. Marini. Unified analysis of discontinuous galerkin methods for elliptic problems. *SIAM Journal on Numerical Analysis*, 39(5):1749–1779, 2002.

[7] C. Canuto, M. Hussaini, A. Quarteroni, and T. Zang. *Spectral methods: Fundamentals in single domains*. Springer, Berlin, 2006.

[8] C. Canuto, M. Hussaini, A. Quarteroni, and T. Zang. *Spectral Methods Evolution to Complex Geometries and Applications to Fluid Dynamics*. Springer series in computational physics. Berlin New York: Springer-Verlag, 2007.

[9] G. Cohen. *Higher-order numerical methods for transient wave equations*. Springer Science & Business Media, 2013.

[10] J. D. De Basabe and M. K. Sen. Grid dispersion and stability criteria of some common finite-element methods for acoustic and elastic wave equations. *Geophysics*, 72(6):T81–T95, 2007.

[11] J. D. De Basabe, M. K. Sen, and M. F. Wheeler. The interior penalty discontinuous Galerkin method for elastic wave propagation: grid dispersion. *Geophysical Journal International*, 175(1):83–93, 2008.

[12] M. Dubiner. Spectral methods on triangles and other domains. *Journal of Scientific Computing*, 6(4):345–390, 1991.

[13] M. Dumbser and M. Käser. An arbitrary high-order discontinuous Galerkin method for elastic waves on unstructured meshes – II. The three-dimensional isotropic case. *Geophysical Journal International*, 167(1):319–336, 2006.

[14] Y. Epshteyn and B. Rivière. Estimation of penalty parameters for symmetric interior penalty Galerkin methods. *Journal of Computational and Applied Mathematics*, 206(2):843–872, 2007.

[15] E. Faccioli, F. Maggio, R. Paolucci, and A. Quarteroni. 2d and 3d elastic wave propagation by a pseudo-spectral domain decomposition method. *Journal of seismology*, 1(3):237–251, 1997.

[16] E. H. Georgoulis, E. Hall, and P. Houston. Discontinuous Galerkin methods for advection-diffusion-reaction problems on anisotropically refined meshes. *SIAM Journla on Scentific Computing*, 30(1):246–271, 2007/08.

[17] T. J. Hughes. *The finite element method: linear static and dynamic finite element analysis*. Courier Corporation, 2012.

[18] G. Karniadakis and S. Sherwin. *Spectral/hp element methods for computational fluid dynamics*. Oxford University Press, 2 edition, 2005.

[19] M. Käser and M. Dumbser. An arbitrary high-order discontinuous Galerkin method for elastic waves on unstructured meshes – I: The two-dimensional isotropic case with external source terms. *Geophysical Journal International*, 166(2):855–877, 2006.

[20] D. Komatitsch and J. Tromp. Introduction to the spectral element method for three-dimensional seismic wave propagation. *Geophysical Journal International*, 139(3):806–822, 1999.

[21] T. Koornwinder. Two-variable analogues of the classical orthogonal polynomials. *Theory and applications of special functions*, pages 435–495, 1975.

[22] I. Mazzieri and F. Rapetti. Dispersion analysis of triangle-based spectral element methods for elastic wave propagation. *Numerical Algorithms*, 60(4):631–650, 2012.

[23] E. Mercerat, J. Vilotte, and F. Sánchez-Sesma. Triangular spectral element simulation of two-dimensional elastic wave propagation using unstructured triangular grids. *Geophysical Journal International*, 166(2):679–698, 2006.

[24] E. D. Mercerat and N. Glinsky. A nodal high-order discontinuous Galerkin method for elastic wave propagation in arbitrary heterogeneous media. *Geophysical Journal International*, 201(2):1101–1118, 2015.

[25] R. Pasquetti and F. Rapetti. Spectral element methods on unstructured meshes: comparisons and recent advances. *Journal of Scientific Computing*, 2006.

[26] A. T. Patera. A spectral element method for fluid dynamics: laminar flow in a channel expansion. *Journal of Computational Physics*, 54(3):468–488, 1984.

[27] A. Quarteroni and A. Valli. *Numerical approximation of partial differential equations*, volume 23. Springer Science & Business Media, 2008.

[28] P. A. Raviart and J. M. Thomas. *Introduction à l' analyse numérique des équations aux dérivées partielles*. Masson, 1983.

[29] B. Rivière. *Discontinuous Galerkin methods for solving elliptic and parabolic equations: theory and implementation*. Society for Industrial and Applied Mathematics, 2008.

[30] B. Rivière, S. Shaw, and J. Whiteman. Discontinuous Galerkin finite element methods for dynamic linear solid viscoelasticity problems. *Numerical Methods for Partial Differential Equations*, 23(5):1149–1166, 2007.

[31] B. Rivière and M. F. Wheeler. Discontinuous finite element methods for acoustic and elastic wave problems. *Contemporary Mathematics*, 329:271–282, 2003.

[32] G. Seriani and S. Oliveira. Dispersion analysis of spectral element methods for elastic wave propagation. *Wave Motion*, 45(6):729–744, 2008.

[33] G. Seriani, E. Priolo, and A. Pregarz. Modelling waves in anisotropic media by a spectral element method. In *Proceedings of the third international conference on mathematical and numerical aspects of wave propagation*, pages 289–298. SIAM, 1995.

[34] P. M. Shearer. *Introduction to seismology*. Cambridge University Press, 2009.

[35] S. J. Sherwin and G. E. Karniadakis. A new triangular and tetrahedral basis for high-order (hp) finite element methods. *International Journal for Numerical Methods in Engineering*, 38(22):3775–3802, 1995.

[36] T. Warburton. An explicit construction of interpolation nodes on the simplex. *Journal of Engineering Mathematics*, 56(3):247–262, 2006.

[37] F. I. Zyserman and P. M. Gauzellino. Dispersion analysis of a nonconforming finite element method for the three-dimensional scalar and elastic wave equations. *Finite elements in Analysis and Design*, 41(13):1309–1326, 2005.

MOX Technical Reports, last issues

Dipartimento di Matematica
Politecnico di Milano, Via Bonardi 9 - 20133 Milano (Italy)

17/2016 Penati, M.; Miglio, E.
A new mixed method for the Stokes equations based on stress-velocity-vorticity formulation

15/2016 Ieva, F.; Paganoni, A.M.
A taxonomy of outlier detection methods for robust classification in multivariate functional data

16/2016 Agosti, A.; Antonietti, P.F.; Ciarletta, P.; Grasselli, M.; Verani, M.
A Cahn-Hilliard type equation with degenerate mobility and single-well potential. Part I: convergence analysis of a continuous Galerkin finite element discretization.

14/2016 Bonomi, D.; Manzoni, A.; Quarteroni, A.
A matrix discrete empirical interpolation method for the efficient model reduction of parametrized nonlinear PDEs: application to nonlinear elasticity problems

13/2016 Guerciotti, B; Vergara, C; Ippolito, S; Quarteroni, A; Antona, C; Scrofani, R.
Computational study of the risk of restenosis in coronary bypasses

11/2016 Zhu, S.; Dedè, L.; Quarteroni, A.
Isogeometric Analysis and proper orthogonal decomposition for the acoustic wave equation

12/2016 Bartezzaghi, A.; Dedè, L.; Quarteroni, A.
Isogeometric Analysis of Geometric Partial Differential Equations

10/2016 Flemisch, B.; Fumagalli, A.; Scotti, A.
A review of the XFEM-based approximation of flow in fractured porous media

08/2016 Dassi, F.; Perotto, S.; Si, H.; Streckenbach, T.
A priori anisotropic mesh adaptation driven by a higher dimensional embedding

07/2016 Pacciarini, P.; Gervasio, P.; Quarteroni, A.
Spectral Based Discontinuous Galerkin Reduced Basis Element Method for Parametrized Stokes Problems